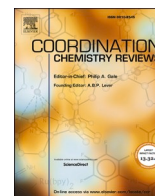Contents lists available at ScienceDirect

Coordination Chemistry Reviews

journal homepage: www.elsevier.com/locate/ccr

Review

Catalytic imaging-guided cancer therapy using non-coordinated and coordinated nanozymes

Mojtaba Falahati [a,b], Majid Sharifi [c,d,*], Yasaman Vahdani [e], Setareh Haghighat [f], Timo L.M. ten Hagen [a,b,*], Yu Cai [g,*]

[a] Precision Medicine in Oncology (PrMiO), Department of Pathology, Erasmus MC Cancer Institute, Erasmus MC, Rotterdam, the Netherlands
[b] Nanomedicine Innovation Center Erasmus (NICE), Erasmus MC, Rotterdam, the Netherlands
[c] Student Research Committee, School of Medicine, Shahroud University of Medical Sciences, Shahroud, Iran
[d] Department of Tissue Engineering, School of Medicine, Shahroud University of Medical Sciences, Shahroud, Iran
[e] Department of Biochemistry and Molecular Medicine, University of Montreal, Canada
[f] Department of Microbiology, Faculty of Advanced Sciences and Technology, Tehran Medical Sciences, Islamic Azad University, Tehran, Iran
[g] State Key Laboratory of Bioactive Molecules and Drug Ability Assessment, Jinan University / International Cooperative Laboratory of Traditional Chinese Medicine Modernization and Innovative Drug Development of Ministry of Education (MOE) of China / Guangdong Key Lab of Traditional Chinese Medicine Information / International Science and Technology Cooperation Base of Guangdong Province / School of Pharmacy, Jinan University, Guangzhou, Guangdong 510632, China

ARTICLE INFO

ABSTRACT

Nanozymes with and without coordinated structures, in addition to performing enzyme-mimic activities through converting $O_2^{\bullet-}$ to H_2O_2 or H_2O_2 into O_2 and $^{\bullet}OH$, are of interest in the development of diagnostic imaging and image-guided therapy platforms. Controlled catalytic activity, high selectivity/sensitivity, low cost, easy generation, stability and biodegradability, and combination therapy, make the use of nanozymes promising for imaging-guided cancer therapy. Therefore, in this review, we attempt to describe the improved imaging resolution relied on the catalytic activity of nanozymes in the TME mediated by the accumulation of contrast agents (such as metal ions, contrast agents, and organic compounds) or molecules that provide the high-resolution imaging of tumor cells. The following section delves into important approaches, including tumor inhibition, nanocarrier clearance, biocompatibility, as well as the efficacy of nanozymes with and without coordinated structures in catalytic cancer therapy. Finally, with an overview of the challenges, we highlighted the main obstacles in the development of nanoscale catalysts in the advancement of multimodal imaging for improved diagnosis and cancer therapy. We hope that this review may clarify the important aspects regarding the utilization of nanozymes, both with and without coordinated structures in multi-modal imaging and image-guided cancer therapy.

1. Introduction

Imaging is a crucial and effective tool in therapeutic perspectives, particularly in tumor therapy, by visualizing biological structures and processes [1]. Using images to diagnose the disease status based on the spatial structure of tumors enables more precise analysis for choosing

between invasive (surgery) or non-invasive (drug administration, radiotherapy, phototherapy) treatment methods [2]. Thus, various imaging techniques like MRI, CT scan, radiography, PET scan, ULS, and FL are constantly being assessed to enhance the signal-to-noise ratio and improve multimodal imaging. Given the biological nature of tumors and limitation of conventional optical imaging tools due to shallow penetration depth, breaking the depth shallow can efficiently augment the imaging-guided cancer therapy. Nanostructures with targeting abilities,
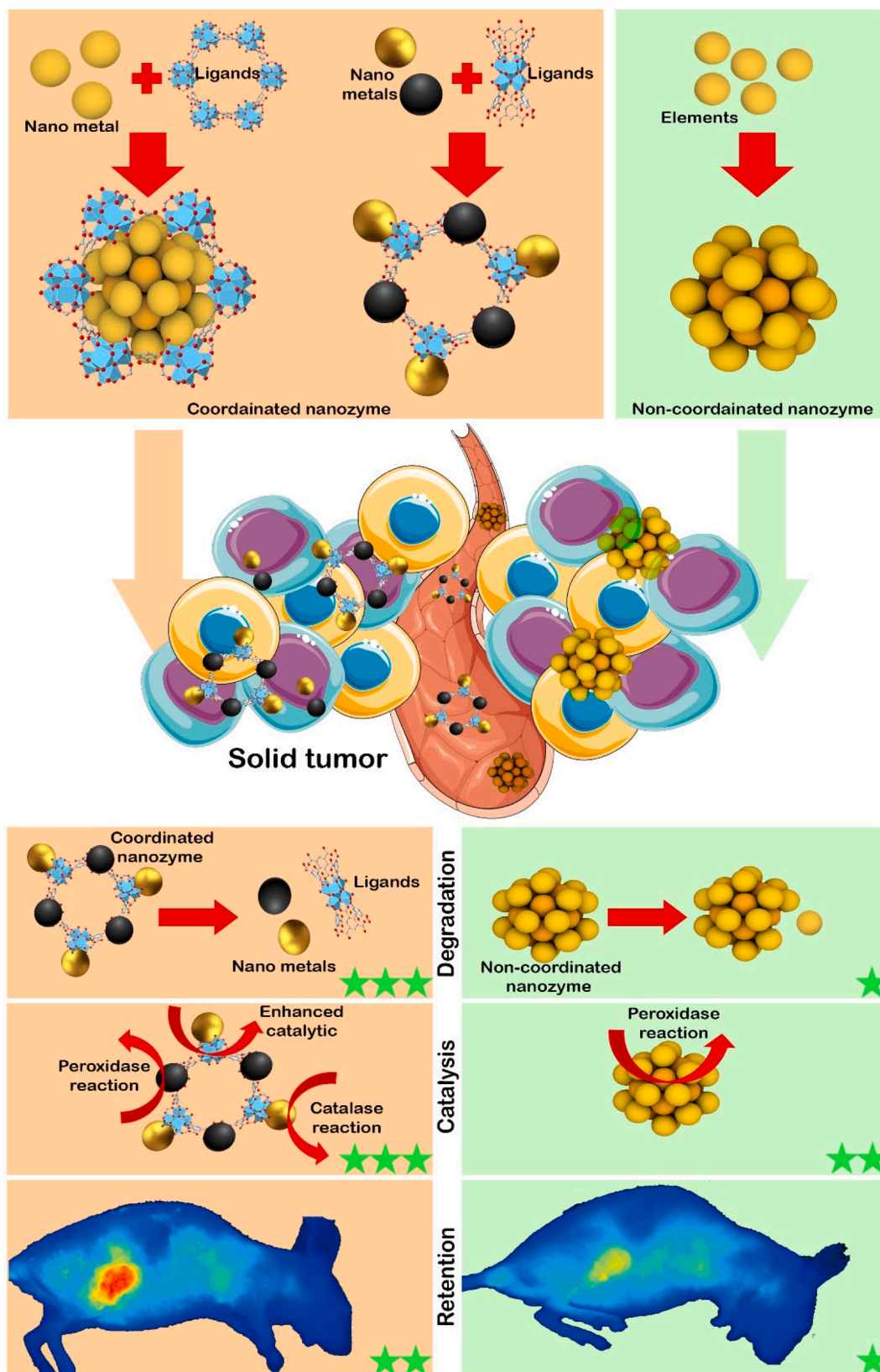

Fig. 1. A schematic view of the structure of coordinated or non-coordinated nanozymes and their applications in catalytic imaging-guided cancer therapy.

high sensitivity, and deep penetration capacity can rapidly facilitate the accumulation of imaging probe within deep-seated tumor with minimal side effects [3,4]. The research process in nanomedicine for tumor imaging and treatment relies on extending the half-life and retention of contrast agents or drugs, targeting and amplifying signals [5,6]. However, the effectiveness of nanostructures in enhancing imaging-guided cancer therapy is partly influenced by the biological characteristics of the TME, including pH, hypoxia, and redox gradients, which have not been specifically addressed. While, elevated hypoxic levels in tumor tissue can interfere with imaging because of decreased permeability of nanostructures, drugs, and contrast agents [5,7]. Moreover, variations in TME chemistry caused by non-uniform aggregation of nanostructures also hinder uniform image quality [8,9]. Nanozymes, nanomaterials with intrinsic enzyme-like activity, have represented potential applications in artificial engineering of intracellular biochemical processes or introducing exogenous responses to enable imaging-guided cancer therapy [10].

Hence, utilizing nanozymes with peroxidase- (produces $^{\bullet}OH$ and $^{\bullet}O_2$ by oxidizing substrates in the presence of H_2O_2), oxidase- (converts O_2 to generate ROS like an H_2O_2 or $^{\bullet}O_2$), catalase- (converts H_2O_2 into H_2O and O_2), and superoxide dismutase- (disproportionate superoxide radicals with O_2 and H_2O_2) like activities is expected to improve the potential for further penetration of drugs and contrast agents mediated by overcoming hypoxia in TME [7,11,12]. In this context, nanozymes not only enhance the permeability of contrast agents in tumors but also alter the chemical composition of the TME by enriching O_2 and H_2O_2, and photosensitive metal ions, thereby significantly affecting image quality [13–17]. Although nanozymes introduce different therapeutic and imaging advantages, their clinical applications are still hindered due to several reasons such as non-targeted distribution, increased cytotoxicity stemmed from cumulative ion release, and unlimited catalytic reactions [9,18]. However, due to their strong surface plasmon resonance, a large number of binding sites, and controllable optical characteristics, nanozymes are very attractive in tumor imaging [19]. Various tactics have been utilized to address the aforementioned challenges, including surface modification, multi-element composition, and particle size reduction [20]. Nevertheless, certain drawbacks have been noted such as a decrease in the number of active sites as a result of surface modification and rapid clearance from the kidney due to size reduction [21]. One important approach to address the clinical applications of these nanostructures is the use of nanozymes with a coordinated structure, where the interaction between the ligand and the nanozyme plays a crucial role in their development (Fig. 1). Improved drug and contrast agent co-loading capacity, feasible combination of therapeutic modalities, active and passive tissue targeting with high retention, and highly control of biocompatible components make coordinated structures promising candidates in biomedicine [22]. Coordinated structures enable miniaturization of nanozymes to enhance their catalytic performance *in vivo* mediated by increasing the number of active sites and improving the EPR effect at the tumor site [23]. Meanwhile, the temporal and spatial degradation of coordinated structures following imaging-guided cancer therapy leads to an increase in the clearance rate of these highly miniaturized nanozymes for overcoming their unwanted side effects [24].

Coordinated structures not only act as carriers for metal ions and ligands to modify the chemical pattern of TME for for an increased imaging resolution by changing the levels of O_2, H_2O_2, and ions [25–29] but also delivering contrast agents along with chemotherapeutics. For instance, high-resolution imaging have been enabled by the application of coordinated structures loaded with Indocyanine green [30]. Likewise, organic ligands such as imidazole [31], Rhodamine B [32], and pyrene group [33] have been shown to serve as imaging reagents because of their potential fluorescent characteristics. Similarly, metal ions like Fe^{3+} [34], Mn^{3+} [35], and Gd^{3+} [36] act as T1- or T2-weighted MRI probes.

In this review we will begin with the introduction of imaging techniques followed by overviewing the mechanism and pros or cons of conventional nanozymes in catalytic imaging-guided cancer therapy. Then, the performance of nanozymes with coordinated structures in catalytic imaging-guided cancer therapy and their advantageous over non-coordinated structures were surveyed. Ultimately, the challenges and potential strategies for developing nanozymes with coordinated structures were emphasized to may put forward the filed in developing the potential clinical applications of nanozymes.

1.1. History

Considering the importance of imaging in cancer treatment, the provision of high-resolution and easy-to-use imaging tools is viewed as one of the most important areas of modern medicine. Despite the significant advances in imaging tools following the discovery of X-rays (1895 CE), the use of nanostructures in imaging transformed the imaging perspective from a diagnostic-analytical approach to a multi-purpose imaging-guided cancer therapy strategy [37]. Nanozymes have recently received a great deal of attention in multimodal imaging-guided cancer therapy (Fig. 2A). However, a significant number of original research indicates that the application of nanozymes with coordinated structures is still in its early stage.

1.2. Facts

- Solid tumors often have areas of chronic hypoxia (due to limited oxygen diffusion distances) or cycling hypoxia (caused by changes in vascular flow and transient perfusion), whose temporal, biological and spatial characteristics should be described in a non-invasive and rapid procedure to increase therapeutic effectiveness [5]. In this regard, nanostructure-based imaging techniques are important due to providing the improved imaging resolution as well as monitoring of hypoxic areas and therapeutic modalities [38].
- Nanozymes with high stability, recyclability, multifunctional and cascade catalytic reactions are of great interest to biomedical implementations due to their unique catalytic sites, manipulated catalytic activity and internal- and external- responsive manner [39]. However, their toxicity due to non-limited reactions and retention in vital tissues has restricted their use.
- MOF nanostructures with high porosity, pH-responsive behavior, and degradability under physiological conditions can prevent the side effects of nanozyme accumulation in tissues by reducing the particle size to less than 15 nm and increasing the filtration rate, in addition to targeted drug loading [40]. However, coordinating their catalytic activities with the rate and site of decomposition remains a main challenge.

1.3. Open questions

- Which nanozyme structure is suited for catalytic cancer therapy and imaging? And by what criteria are they evaluated in biomedical applications?
- What factors determine the choice of the mechanism of action and type of nanozyme in imaging?
- What is the most strategic approach to control nanozyme toxicity in cancer imaging and therapy?
- What are the most important challenges and opportunities associated with the use of nanozymes in cancer imaging-guided therapies?

2. Imaging techniques

Imaging devices and objectives are two critical components for rapid diagnosis. Although there is a wide variety of imaging devices, statistical trends exhibit that researchers are paying more attention to CT scans (50.18 %), MRI (23.61 %), and PET scans (15.44 %) methods in tumor imaging (Fig. 2B). Nevertheless, imaging modalities recommendations vary according to their advantages and disadvantages in diagnosing and
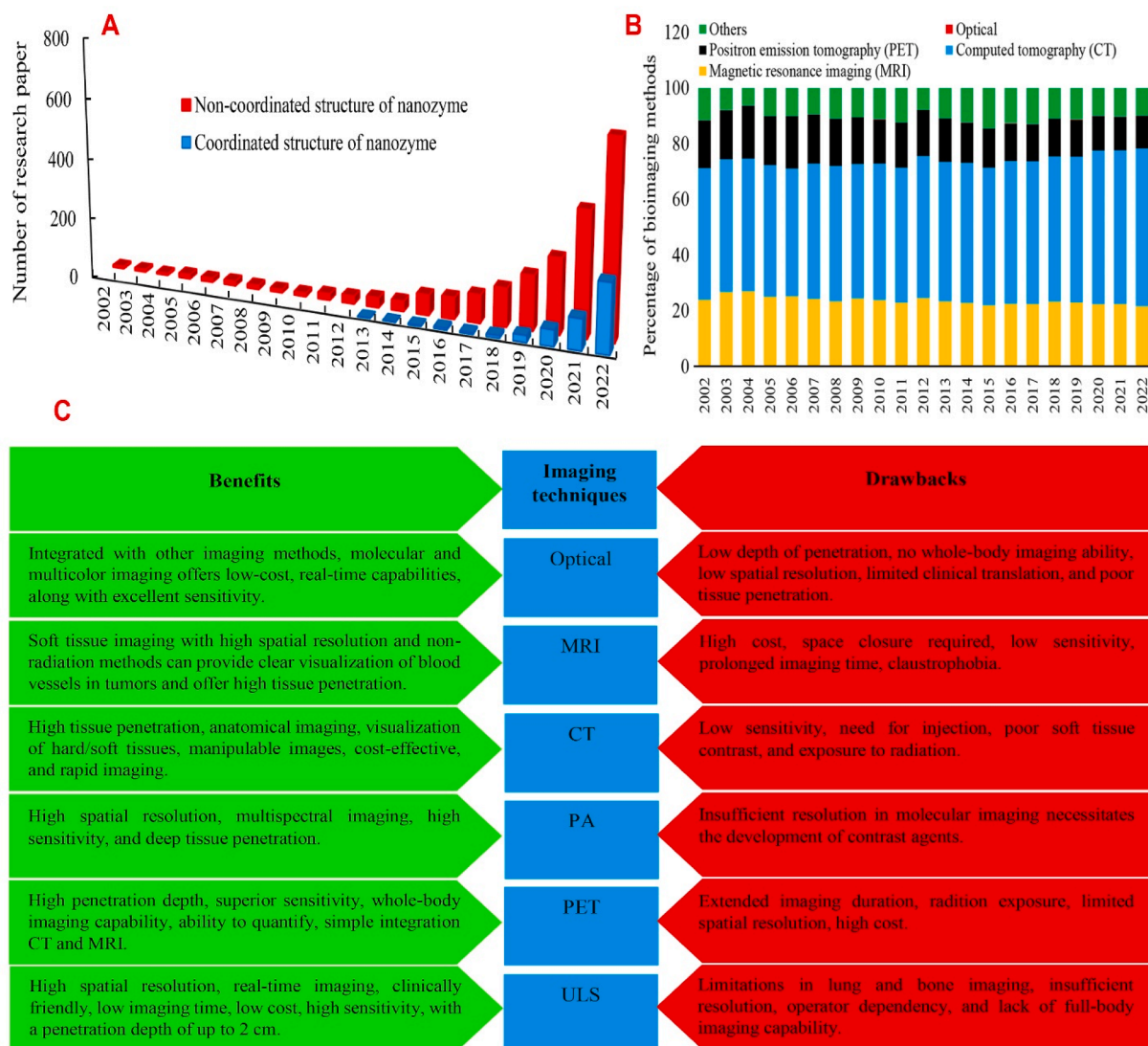
Fig. 2. Chronological increase in the scientific interest in tumor imaging and therapeutics based on nanozymes with and without coordinated structures documented by Scopus, PubMed and Web of Science reports: (A) The number of papers on imaging-guided cancer therapy using nanozymes with and without coordinated structures published from 2002 to 2022, (B) ratio of different imaging perspectives, and (C) advantages and disadvantages of imaging techniques.

targeting tumors (Fig. 2C). Among imaging modalities, MRI is one of the methods of interest in imaging-guided cancer therapy due to its high spatial resolution, excellent contrast especially for soft tissue, and multidirectional imaging with minimal tissue damage [41]. However, the long relaxation time of water protons still makes it puzzling to distinguish between benign and malignant tumor tissues. Using a contrast agents manipulating the proton relaxation rate is thought to be crucial in addressing this concern [41,42]. PA imaging could be used in effective cancer imaging via an enhancement in speed, depth, and resolution enhancement in a second infrared window (1000–1700 nm) [43]. Using a laser as to induce imaging-guided PTT/PDT enhances ULS generation through thermoelastic tissue expansion. Meanwhile, the application of PA technique in tumor visualization is highly intriguing due to the feasible integration of PA imaging and PTT. The use of PET imaging is very important to overcome tissue imaging depth limit [44,45]. High sensitivity (in the pM range) and quantification of the signal for further investigation are two main advantageous of this approach [45], which can be maximized by using nanozymes. Despite the advantages of imaging modalities described above, especially for combined approaches such as PET/CT and PET/MRI, optical imaging is considered to be one of the most important molecular imaging

modalities [46]. Nonetheless, some of the major obstacles to optical imaging continue to include light scattering, inherent FL, and absorption by nearby tissue and surrounding water [47]. Although FL, bioluminescence, and optical tomography imaging techniques have discussed to be effective in developing optical strategies, the use of these approaches in animals has been widely reported.

Additionally, transition plans for research to clinical practice are slowed down, particularly over an extended period of time, by the toxicity of contrast agents or their carriers, which are more important than potential tumor imaging. However, compared to 100 years ago, today's CT scan can detect lung nodules less than 5 mm in size [48], allowing faster and more accurate diagnosis of tumors. Meanwhile, the use of signal enhancement approaches such as temperature elevation as well as magnetic or electrical, and radiant power modulation in clinical applications might pose some drawbacks [49,50]. Although, in laboratory scales, the wide choice of contrast agents, especially the use of nanostructures, overcomes the limitation of imaging improvement [51], these approaches might do not deal with well in clinical practice due to tissue imaging depth limit and insubstantial access time to the contrast agents within the target tissue based on filtration rate and blood flow velocity. Moreover, in laboratory research, the conjugation of dyes with

proteins in the native form or associated nanostructures enables the formation of photostable dyes which is an important factor in tumor imaging [52]; while in clinical practice, the labeling causes some changes in protein function or its removal during biological implementations. Therefore, the development of high-resolution imaging approaches in laboratory research, is currently substantially incompatible with imaging modalities in clinical cancer research. However, reporter gene imaging in preclinical and clinical studies has been reported in cancer diagnosis. Of course, the possibility of interfering unexpected pathways limits the use of reporter genes in clinical applications [53]. In general, the use of imaging equipment is not recommended equally for everyone, derived from the importance of personal medicine. As a result, it is imperative to integrate computational techniques, refine imaging methodologies, enhance contrast agents, and explore novel imaging strategies.

3. Non-coordinated nanozymes in tumor imaging

By changing the imaging approach from anatomical- to anatomical-functional mode, it became possible to visualize tumor structures even in the early stages [54]. Functional imaging based on molecular responses seems to not only provide insight into physiological changes during treatment but also enable rapid cancer diagnosis [54,55]. Whereas, visualizing the events in a functional form in order to create an anatomical guide and developing associated treatment strategies is challenging, especially in the early stages of cancer. For this purpose, the use of multifaceted materials such as nanostructures with the ability to perform imaging-guided cancer therapy is recommended [56]. Despite the limited clinical application of nanostructures in imaging, there are numerous laboratory research reports on application of biomedical nanostructures for imaging-guided cancer therapy [57]. The use of metal NPs is of great interest due to their strong absorption spectra, high stability and tunable physicochemical properties [58]. However, the most important indicators of being a nanostructure's friend or foe as an imaging agent are their corresponding safety in off-target tissues and biocompatibility. Therefore, it is crucial to artificially manipulate their toxicity and biodegradation in biomedical applications. Among NPs, the use of nanozymes with several unique functions such as drug delivery, photo/chemo combination therapy, ratiometric molecular imaging, and hypoxia manipulating properties in solid tumors for enhancing therapeutic/imaging agent penetration have received a lot of attention in the development of promising NPs for imaging-guided cancer therapy (Table 1) [59]. However, the unlimited catalytic reactions/unwanted reactions in physiological environment impose major challenges to the biological application of nanozymes [60,61]. Despite the advancement of potential strategies to overcome the unwanted toxicity of nanozymes such as surface modification and coatings [21], the application of developed nanozymes in preclinical and clinical settings remains unknown. The establishment of tunable inducers (temperature, acidity, light) to control catalytic activity and the development of degradation-based strategies associated with application of alloy or composite nanozymes appear to be very promising [62]. However, reconciling all medical requirements such as imaging, permeability enhancement and drug delivery with physiological and environmental compatibility is complicated and, in some cases, impossible. Nonetheless, the potential to improve the signal-to-noise ratio in solid tumors and increase the penetration of contrast agents enabled by nanozymes will draw attention to the use of these compounds in the near future.

Considering the catalytic mechanisms, 4 general classes of nanoscale catalysts are categorized as redox (oxidant and antioxidant enzymes), hydrolytic (cleavage towards phosphate bonds, amide bonds, and glycoside bonds), biorthogonal (through coupling and uncaging reactions), and multi-enzymes [63,64]. However, depend on the mechanism of action of nanozymes in imaging-guided cancer therapy, they can be divided into two classes: (1) images obtained from the intrinsic properties of nanozymes, and (2) images obtained from the performance of the nanozymes on contrast agents. The primary limitations of the initial procedure include the constrained availability of nanozyme sources with specific absorption and emission spectra, maintaining the stability of emission spectra without altering catalytic activity during imaging, and ensuring the complete accumulation of nanozymes within the target tissue to prevent potential side effects [65]. While the major drawbacks of the second approach are the complexity of the imaging procedure due to the essential and simultaneous presence of the contrast agent and the nanozymes, the uncontrolled and differential penetration of the contrast agent into different parts of the solid tumor, and the lack of reliability of intrinsic chromogens in cancer tissue.

3.1. Peroxidase-based tumor imaging-guided cancer therapy

More than 40 nanostructures with peroxidase-like activity have been identified, including iron NPs, especially iron chalcogenides [FeS NPs, FeSe NPs], iron phosphates and doped ferrites [$CoFe_2O_4$ and $BiFeO_3$], vanadium compounds, and carbon nanostructures [78]. In addition to peroxidase activity, metal NPs and their oxides can simultaneously show catalase-like activity [79]. The primary factor

Table 1
An overview of the use of nanozymes in imaging-guided cancer therapy.

Catalytic Mechanism	Nanozyme	Size (nm)	Model	Imaging	Tumor state
Peroxidase	Pd-Cu-Fe-NEs [14]	5.46 ± 0.79	4T1 tumor-bearing mice	FL	Tumor weight reduction: 5–6 folds with PTT and ultrasound
Peroxidase	CuPP@PEG [66,67]	~100	4T1 tumor-bearing mice	FL	Tumor weight reduction: 3–4 folds with αPD-L1 or US
Peroxidase	Fe@Fe$_3$O$_4$@heparin [13]	13.3 ± 0.1	4T1 xenograft model	MRI	Tumor weight reduction: 3–5 folds
Peroxidase	Fe$_3$O$_4$/Pt-FLU@PEG [17]	100 ± 2.26	4T1 tumor-bearing mice	PA	Tumor weight reduction: 1.5–2.5 folds
Peroxidase/catalase	PtFe@Fe$_3$O$_4$ [15]	5–20	Pancreatic cancer model	PA/CT	Tumor weight reduction: 4–5 folds with PTT
Peroxidase-oxidase	AuPt@SF [68]	~120.3	4T1 xenograft model	FL/PA	Tumor weight reduction: 1.5–2.5 folds
Peroxidase	Ag$_2$S@Fe$_2$C-DSPE-PEG-iRGD [69]	≤ 25	4T1 tumor–bearing mice	MRI/FL	Tumor weight reduction: 4–6 folds with PTT
Peroxidase/catalase	PEG/Ce-Bi@DMSN [70]	$10 \pm 4 \times 60 \pm 15$	U14 tumor xenografts	CT	Tumor volume reduction: 6–9 folds with PTT
Peroxidase	PEG/Fe$_5$C$_2$@Fe$_3$O$_4$ [71]	~20	4T1 tumor-bearing mice	MRI	Tumor volume reduction: 8–12 folds
Catalase	RuO$_2$@BSA [72]	3.5–7.5	4T1 tumor-bearing mice	FL	Tumor weight reduction: 3–5 folds with PTT/PDT
Catalase	PtBi-β-CD-Ce6 [16]	~101.3	U14 tumor-bearing mice	PA/CT	Tumor weight reduction: 3–6 folds with PTT/PDT
Catalase	PtPB [73]	~110	4T1 tumor-bearing mice	PA	Tumor volume reduction: 6–8 folds with PTT
Catalase	PANI/PPy@Au @MnO$_2$ [74]	~120	MCF-7 tumor-bearing mice	MRI	Tumor volume reduction: 6–8 folds with PTT/CDT
Catalase	AuNCs@mSiO$_2$@MnO2 [75]	~140	MDA-MB-435 tumor nude mice	MRI	Tumor volume reduction: 5–7 folds with PDT
Oxidase	CoO@AuPt [76]	~36	4T1 tumor-bearing mice	PA/CT	Tumor volume reduction: 2–3 folds with PDT
Glutathione peroxidase	Ava@SPIOs [77]	~18	MDA-MB-231 tumor xenograft	MRI	Tumor volume reduction: 4–5 folds

influencing the shift in nanozyme activity from peroxidase to catalase is the pH change [38]. The TME exhibits several unique characteristics such as acidity, hypoxia, inflammation, and H_2O_2 overproduction that distinguish it from the adjacent tissues [5]. Therefore, the application of nanozymes with peroxidase-like activity in this environment could play a crucial role in catalytic cancer imaging and therapeutic perspectives.

For example, using $Fe_3O_4@CS/CuS$ nanocomposites with dimensions of 50 to 100 nm, Zhang et al. [80] reported the multimodal imaging of lung tumor, in addition to the apoptosis induction through synergistic peroxidase-like activity with PDT. $Fe_3O_4@CS/CuS$ NPs with a half-life of 8 h and a two-chamber clearance model, act as a highly stable contrast agent to enhance the imaging signal. Fe3O4@CS/CuS improves contrast
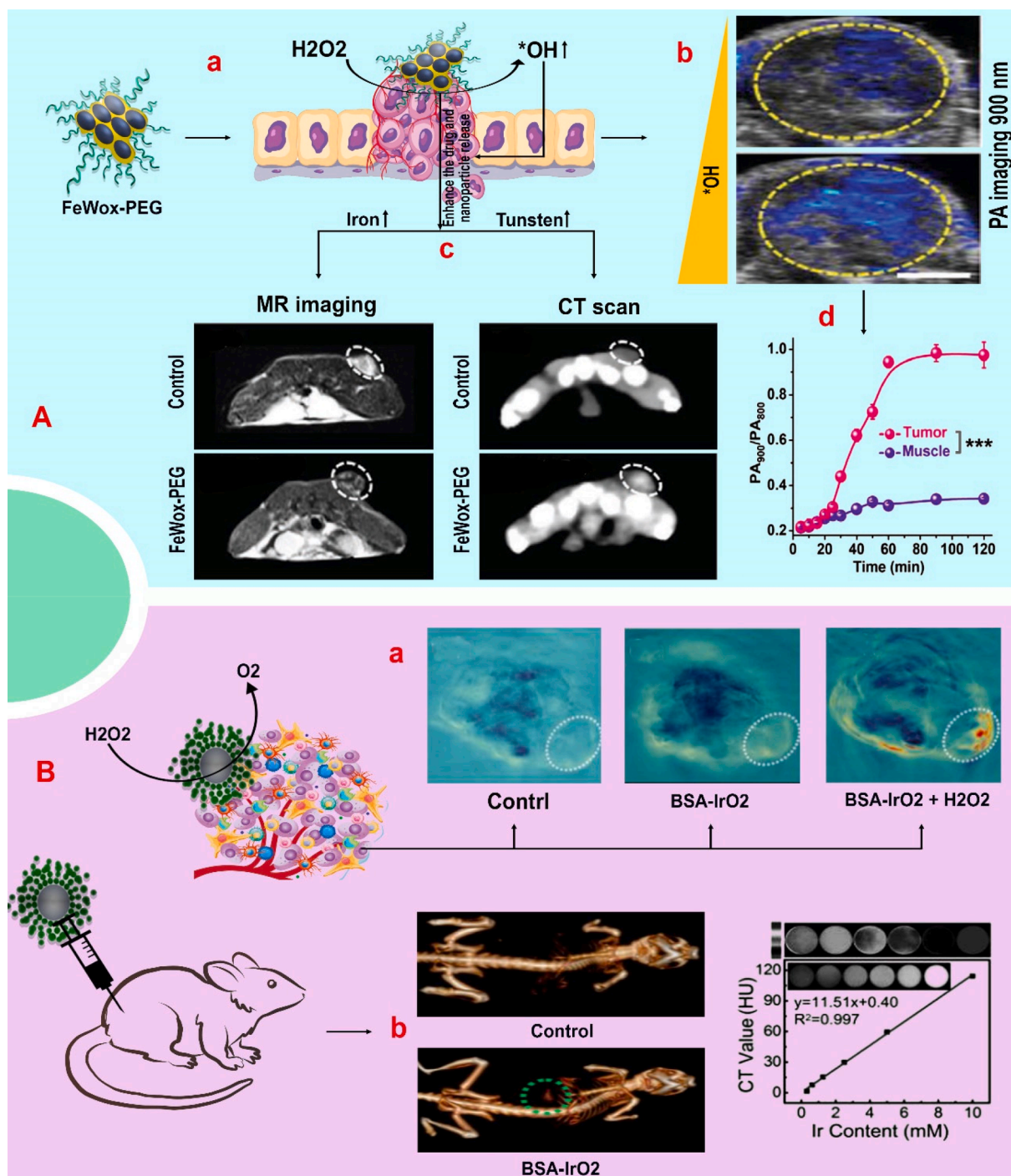

Fig. 3. A) Schematic illustration of FeWO$_X$-PEG nanozyme application in 4T1 xenograft tumor imaging (a). The effect of OH resulting from the accumulation and destruction of H_2O_2 on PA imaging of 4T1 xenograft tumor after FeWO$_X$-PEG injection (b). The effect of releasing iron and tungsten ions due to catalytic activity on MRI and CT imaging in control and FeWO$_X$-PEG-treated mice at 24 h (c). The reduction of PA900/PA800 ratios for muscle tissue compared to 4T1 xenograft tumor at different times after FeWO$_X$-PEG injection indicates targeting and EPR effect of nanozyme based on H_2O_2 detection (n = 3 biologically independent samples). Reprinted with permission from Ref. [83], with permission from John Wiley. Copyright (2020) John Wiley. B) The effect of using BSA-IrO$_2$ in PA imaging of HeLa-tumor in the presence and absence of H_2O_2 (a). Diagram of concentration-dependent CT signals *in vitro* by determining the Hounsfield unit values of BSA-IrO$_2$ solutions along with CT images before and following injection of BSA-IrO$_2$ NPs at 12 h (b). Reprinted with permission from Ref. [90], with permission from John Wiley. Copyright (2018) John Wiley.

agent permeability caused by a rise in O_2, which improves imaging resolution, in addition to enhancing FL intensity by increasing $^•OH$. Animal models, showed that the nanocomposites efficiently converted light irradiation (980 nm laser spectrum) into heat within 5 min (up to 50 °C), enabling higher resolution PTI than conventional methods (at a temperature of 38–39 °C). Nonetheless, the accumulation of $Fe_3O_4@CS/CuS$ NPs in off-target tissues, especially the liver, lung and kidney, which was confirmed by PLI within 12 h, makes it complicated to perform imaging-guided cancer therapy [80]. As a consequence, a prerequisite for using nanozymes in biomedical applications is a rapid filtration rate and safety, despite the enhanced contrast and improved signal-to-noise ratio in imaging modalities. For this purpose, Ding et al. [81] by developing exosome vesicles containing ABTS and graphene quantum dot nanozymes (10 nm), were able to improve the resolution of PA imaging in nasopharyngeal tumors up to 10-fold, focusing on reducing the nanozymes toxicity. Oxidized ABTS by nanozyme is known to be a highly potent contrast agent. Imaging by this approach is relied on contrast agents resulting from nanozymes performance rather than on the nanozyme chemical structures. Accordingly, the toxicity of the nanozymes used is greatly reduced due to (1) lower doses and (2) less accumulation in off-target tissues resulting from erythrocyte-derived exosome membranes. However, the main limitation of this strategy is the inability to perform multimodal imaging of oxidized materials [81]. In addition to reducing the prescribed doses, degradable nanozymes and particle size reduction are important factors to improve imaging resolution and reduce toxicity. Hence, due to the biocompatibility of calcium and iron, CaO_2-$Fe_3O_4@HA$-Cy7 exhibited special tracking and imaging capabilities in addition to therapeutic efficacy derived from potential drug delivery and ROS enhancement [82]. CaO_2-$Fe_3O_4@HA$-Cy7 effectively improved the quality of Cy7-based FL images 12 h after injection by enhancing the $^•OH$ content derived from the catalytic activity of Fe_3O_4 at pH 6. On the other hand, FL quenching over 24 h indicates the gradual destruction of nanozyme and consequent cytotoxicity modulation. Meanwhile, Fe_3O_4 NPs in CaO_2-$Fe_3O_4@HA$-Cy7 as a sensitive T_1 MRI contrast agent with corresponding longitudinal relaxation (r_1) at a concentration of 4.17 mM showed excellent performance in enhancing MRI resolution within 8 h after injection. The FL signal reached a maximum at 12 h following injection and the MRI signal decreased after 8 h, which can be taken as an indicator of nanozyme degradation [82]. Additionally, Gong et al. [83] developed degradable FeWOX-PEG bimetallic nanozyme with a high affinity for H_2O_2 (K_m: 3.26×10^{-3} M) and excellent catalase-like activity, V_{max}: 423×10^{-8}. FeWOX-PEG nanozyme by generating $^•OH$ enables targeted PA imaging in normal H_2O_2 concentration with minimal side effects and maximum resolution between 20 and 60 min (Fig. 3A). The clearance rate and biodegradability of the bimetallic nanozyme FeWOX-PEG were significantly high, despite great accumulation in the liver and spleen. The bimetallic nanozyme FeWOX-PEG not only facilitates intracellular ROS and apoptosis in breast tumors but also enables multimodal imaging following intravenous injection (Fig. 3A). One of the advantages of imaging enabled by FeW-X-5 is the enhancement of FL intensity due to increased $^•OH$, and 2.5- and 1.9-fold enhancement of CT and MRI images derived from enhanced tungsten and iron release triggered by $^•OH$. Tungsten and iron have strong X-ray affinity and T_2 shortening rates (r_2: 1.21×10^{-3} m/s) respectively, which are effective to provide improved imaging resolution [83]. However, the potential for nanozymes-mediated cancer catalytic therapy is hampered due to coating modifications or premature degradation. For this purpose, Veroniaina et al. [84] and Jana et al. [14] respectively, by $MnO_2@$heavy-chain apoferritin combined with doxorubicin (DOX, K_m: 5.23 mM and V_{max}: 28.87×10^{-6} M/s to H_2O_2) and integrated PTT (1.0 W/cm^2 5 min) or ultrasonic (0.5 W/cm^2, 1 MHz, 50 % on/off cycle) on a trimetallic (Pd, Cu, and Fe) alloy nanozymes were able to enhance the resolution of MRI (r_1: 33.40 mM/s) and FL imaging of tumor tissue during treatment by increasing permeability with overcoming hypoxia. In another study, it was revealed that AgPd plasmonic blackbody improved the resolution of

CT imaging and the possibility of accurate visualization of uterine tumor, with a 7-fold reduction in U14-tumor volume hinged on synergy with PTT in a wide spectrum (400–1300 nm with an efficiency of 45.1 % in the 1064 nm) [85]. Contrast enhanced CT imaging deriving from HU results is associated with AgPd PB nanozyme concentration, whereas, the enhanced resolution of PA and FL imaging is likely due to the increased $^•OH$ and O_2 resulting from the synergistic effect of peroxidase-like activity and PTT enabled by the developed nanozyme. The PTT-induced change in V_{max} from 2.45 to 4.41 mg/min and change in K_m from 12.87 to 10.14 mM indirectly affects PA imaging by degrading H_2O_2 to O_2. Hence, AgPd PB plays a key role in multimodal imaging directly as a contrast agent in CT imaging and indirectly through a peroxidase-like reaction in PA imaging. Quenching of the FL intensity at 12 and 24 h, respectively, and the absence of PA imaging at 8 h indicate the probable destruction and clearance of nanozymes from the liver (80 %) and kidney (10 %). Furthermore, histopathological results and the low concentration of nanozymes in main tissues raised hope for the modulation of nanozyme toxicity [85]. By developing PtSn@PEG bimetallic nanozymes with superior light absorption and high affinity to H_2O_2 (K_m: 74.13 mM) and appropriate catalase-like activity (V_{max}: 13.65×10^{-8} mM/s), Zhu et al. [86] recently demonstrated that combining peroxidase-like activity with PTT, in addition to improving CT imaging resolution (HU: slope of 6.21) with increased X-ray absorption and enhancing PA imaging intensity through overcoming hypoxia, caused a 5-fold reduction in breast tumor volume without significant tissue toxicity. Despite the high accumulation of nanozymes in the liver and spleen, the bimetallic PtSn@PEG nanozymes appear to be almost safe due to their high clearance rate demonstrated by a two-compartment model and a half-life of 4–6 h [86].

3.2. Catalase-based tumor imaging-guided cancer therapy

A catalase-like reaction is expected to increase the permeability of therapeutic or contrast agents by increasing the levels of O_2 and H_2O [38]. In general, metals and metal oxides exhibit high catalytic activity depending on the conditions of the TME, such as the simultaneous peroxidase and catalase reactions, and play an effective role in cancer therapy. Similar to the peroxidase reaction, pH and temperature could affect the kinetics of the catalase reaction [87]. Among metal NPs, platinum (Pt), palladium (Pa), iridium (Ir), and cobalt (Co) along with zirconium (Zr) nanostructures show superior catalase-like reaction [88]. For instance, to improve X-ray absorption in H_2O_2-rich tumors, Feng et al. [89] designed a nanoscale Ir@liposome catalyst (~100 nm) with a high affinity for H_2O_2 (K_m: 132 mM), which by combination of PTT (0.8–1 W/cm^2) and radiotherapy (140 keV, doses: 6 Gy), reduced breast tumor volume by 5.5- and 4-fold, respectively. Although the PA signal from iridium (~3.3 nm) increases linearly with increasing concentration up to 5 mg/mL, the gradual increase in PA signal over 8 h at a constant concentration can be attributed to the high accumulation of nanozyme in the target tissue and the enhancement of the O_2 level enabled by the catalase-like reaction. Despite the high accumulation of Ir@liposome in the liver and spleen tissues, and less accumulation of Ir@liposome in the heart, kidney, lung, skin, muscle, and gastrointestinal tissues, there is growing hope that liposomes can reduce toxicity [89]. To further reduce the accumulation of NPs in off-target tissues and reduce their toxicity, Zhen et al. [90] synthesized a BSA-IrO_2 NP (~80 nm) using a one-step synthetic approach. The BSA-IrO_2 nanozyme, in addition to its highly efficient PTT, significantly prevented nanozyme accumulation in the main tissues. The catalase-like reaction of BSA-IrO_2 in combination with PDT and PTT not only reduced the U14-tumor volume by 4-fold and 5-fold, respectively, compared to the control group but also enhanced tissue O_2 levels, thereby improving the performance of PA and CT imaging (HU value: 72.2 in BSA-IrO_2 vs. 43.8 in control). Injecting H_2O_2 into tumor tissue and increasing O_2 levels by BSA-IrO_2 was shown to significantly increase the intensity of PA imaging, demonstrating the effect of catalase-like activity on PA imaging (Fig. 3B) [90]. Besides

coatings that reduce the toxicity of nanozymes, another promising approach is the use of nanozymes with very reduced dimensions to be filtered from major tissues by kidney and liver. In this context, Dan et al. [91] by synthesizing AuNC-ICG (Gold nanocluster- Indocyanine green: size of 1 nm) with a strong affinity to H_2O_2 (K_m: 2 mM) and significant catalase-like activity (V_{max}: 4.55×10^{-3} mM/s), displayed a reducing nanozyme toxicity as well as multimodal imaging –guided PDT (0.3 W/cm^2, 30 min: ~5-fold 4T1 tumor volume reduction) and radiotherapy (8 Gy, 2 Gy/min: ~3-fold 4T1 tumor volume reduction). Despite the stability and long-term circulation of AuNCs-ICG and their relative accumulation in the liver and kidney, the biodistribution results showed that the Au accumulation in the tissues was time-dependent and reached the highest level at 12 h following injection. The prominent reduction of gold concentration in the tissues within 24 h confirms the rapid and efficient filtration of Au by the kidney and liver. Moreover, the output signal-to-noise ratio in FL imaging shows a 3.6-fold increase in the AuNCs-ICG-treated group compared with the ICG alone group. On the other hand, improvements in PA imaging and CT indicate an increased O_2 level (~19.7 % vs. ~ 2.5 %) and further accumulation of AuNPs in breast tumor tissue due to targeted therapy enabled by BSA-containing NPs [91]. In agreement with this finding, Zeng et al. [92] used 3–5 nm cerium oxide nanozymes on a platform made of polyethylenimine, 4-carboxylphenylboronic acid and hyaluronate (ICG@PEI-PBA-HA/CeO$_2$: with a range of 80–200 nm) to achieve a catalytic cancer therapy [10-fold decrease in tumor volume with PTT/PDT (1 W/cm^2, 4 min)] and imaging without an apparent toxicity. In addition, it was found that the developed nanozyme significantly improves the resolution of PA imaging by increasing O_2 levels attributed to catalase activity within the tumor tissue by 2.5-fold (at 6 h) and 3.2-fold (at 24 h) [92].

Bimetallic nanozymes can provide greater improvements in providing increased imaging resolution and catalytic cancer therapy through dual-modal enzyme-like activities. Therefore, the use of these compounds has recently attracted a great deal of interest. For example, SnFe$_2$O$_4$ nanozyme combined with PTT/PDT (0.5 W/cm^2 with conversion efficiency: 42.3 %) caused generation of significant content of O_2, glutathione depletion, and ·OH production, resulting in an efficient catalytic cancer therapy and precise targeting due to pronounced H_2O_2 degradation [93]. The SnFe$_2$O$_4$ platform holds great promise for toxicity modulation by enabling iron-induced magnetic conduction and facile renal filtration with a particle size dimension below 13 nm. Outcomes of ICP-MS by measuring iron level in the tumor site and urinary secretions for 14 days, demonstrated the reduced accumulation of nanozyme in off-target tissues and the absence of pathological effects in the major tissues such as the liver and heart. It appears that the degradation of H_2O_2 to OH and O_2 deduced by catalase-like activity of developed nanozyme may improve CT imaging resolution by increasing intratumoral HU (from 19.4 ± 2.3 to 348.1 ± 1.5). Catalytic activity also releases further iron ions, making SnFe$_2$O$_4$ as an effective contrast agent with a high transverse relaxation value (228.90 mM/s) compared to commercial contrast agents, increasing the MRI signal-to-noise ratio (1.2-fold control). Consequently, SnFe$_2$O$_4$ is not only promising as a CT/MR imaging contrast agent for cancer diagnosis but also plays an effective role in imaging-guided cancer therapy by increasing ROS and improving O_2 levels [93]. In the following, Wang et al. [94] by using a PEGylated bimetallic Au$_2$Pt nanozyme, in addition to reducing K_m (7.7066 mM) and increasing V_{max} (90.18×10^{-8} M/s), which causes high sensitivity to H_2O_2 substrate for O_2 generation, were able to provide high permeability of therapeutic compounds to U14 tumor cells without toxicity to vital tissues. No changes in blood parameters (ALT, AST, ALP, BUN, and CREA), lack of structural damage in the off-target tissues and no weight loss in mice confirm that nanozymes have no or negligible toxicity. While, the synergistic effects of Au$_2$Pt-PEG-Ce6 with PDT (0.25 W/cm^2, 5 min) and PTT (1.0 W/cm^2, 5 min) reduced U14 tumor volume by 8-fold and 10-fold, respectively, raising hopes for catalytic cancer therapy. Furthermore, the increasing HU with a slope of 20.28 ml/mg derived from elevating Au$_2$Pt-PEG-Ce6 concentration and enhancing the

O_2 content within U14-tumor tissue improved the resolution of CT imaging and the signal-to-noise ratio of PA imaging by Au$_2$Pt with dual-modal peroxidase/catalase-like activities [94]. Additionally, regardless of the type of disease, Sun et al. [95] were able to completely block the catalytic activity of nanozyme by depositing an acoustically sensitive mesotetra (4-carboxyphenyl)porphyrin coating (T790) on Pd@Pt. After confirming the presence of Pd@Pt-T790 in the target tissue by the sonodynamic properties of T790, Pd@Pt showed catalase-like activity to catalyze the conversion of H_2O_2 to O_2 and H_2O. No changes in blood parameters (ALT, AST, ALP, BUN, and CREA) and no pathological damage in off-target tissues indicate the potential efficacy of the "blocker and activator" in controlling Pd@Pt nanozyme toxicity and possible side effects. Moreover, acoustically-induced catalytic activity further enhanced the resolution of PA and MRI imaging by enhancing ambient O_2 compared to non-acoustically-induced Pd@Pt nanozymes [95]. Although catalytic cancer therapy of bimetallic nanozymes in tumor tissue is relied on a concentration-dependent manner, the proportion of alloying elements in nanozymes could be effective on catalase-like activity and the resulting imaging. In this way, Carregal-Romero et al. [96] found that changing the formulation of the nanozymes from Mn$_{0.35}$Fe$_{2.65}$O$_4$ to Mn$_{0.95}$Fe$_{2.05}$O$_4$ with dimensions of 10–25 nm increased T_1 and T_2 values following administration. Increasing the ratio of manganese to iron in the developed alloy improves the contrast of MRI imaging. Although both nanozymes have the same affinity for H_2O_2 and its decomposition, the use of Mn$_{0.95}$Fe$_{2.05}$O$_4$ with adjusted magnetic properties may result in superior differential positive contrast or dual-modal T_1/T_2 MRI contrast due to increased O_2 and H_2O contents and possibly enhanced iron ion release. Despite the same clearance rates of both nanozymes by kidney and liver, the 2.8-fold accumulation of Mn in the liver caused by Mn$_{0.95}$Fe$_{2.05}$O$_4$, regardless of dose-dependent toxicity, can cause pathological changes in the liver by inducing pinocytosis/necrosis and inflammation. In addition, the results of the PET scan with ^{68}Ga radiolabel confirmed that the liver was a critical organ for the removal of both nanozymes [96].

Recently, Wang et al. [97] found that incorporation of gadolinium on PEGylated mesoporous silica structures containing DOX (MSNs-PB-Gd-DOX-PEG) further increased the catalase-like activity of PB to 4-fold over normal conditions for imaging. PB as a MRI imaging contrast agent has limited relaxation effects in clinical settings despite its high spatial resolution and remarkable permeability. The use of Gd not only enhances T_1/T_2 dual-modality imaging capabilities but also increases r_1 relaxation by 2-fold (4.55 mM/s) and increases r_2 by 3-fold (8.1 mmol/s) compared to clinical contrast agents and PB, respectively. This higher relaxation efficiency promises improved MRI imaging resolution at lower doses in practical settings due to enhanced catalase-like activity. Modification of nanozymes with folic acid has become a major targeting strategy in reducing the toxicity of manufactured nanozymes. Accumulation of MSNs-PB-Gd-DOX-PEG functionalized by folic acid in tumor tissue deduced by FL imaging along with different assays such as blood parameters (ALT, AST, ALP, BUN, and CREA), liver and kidney function, inflammation, and clearance from lung, spleen and heart tissues confirmed the targeting efficiency and compatibility of the functionalized nanozymes. Furthermore, a 3.5- to 4-fold reduction in tumor volume is expected due to the controlled release of DOX and free radical formation resulting from the destruction of H_2O_2 within the tumor tissue, especially when it was combined with PDT [97].

3.3. Oxidase-based tumor imaging-guided cancer therapy

Insufficient H_2O_2 in some types of cancer complicates catalytic cancer therapy [98]. Therefore, exploiting an oxidase-like reaction that converts O_2 as an electron acceptor to H_2O_2 to form ROS within the tumor tissue is considered as a main strategy to address this drawback [99]. In this regard, Jiang et al. [100] synthesized melanin-containing MnO$_2$-Au nanozymes (MMF-Au) with dimensions of 140–160 nm to enhance H_2O_2 levels in low-H_2O_2 HeLa tumors due to the oxidase-like

activity of AuNPs (~10 nm). MnO_2 facilitated imaging-guided cancer therapy by degrading H_2O_2 to O_2 and $\cdot OH$ (Fig. 4). Moreover, the combined oxidase-like activity of MMF-Au and PTT (0.6 W/cm^2 for 10 min) not only significantly increased the H_2O_2 levels but also reduced the tumor volume by 4-fold compared to the MMF-Au group without causing inflammation or toxicity in off-target tissues. The 2.30-fold and 6.97-fold increases in MRI and PA signal intensity respectively, following application of MnO_2 further indicate the efficacy of nanozyme in imaging low-H_2O_2 tumors [100]. Previously, Teng et al. [101] by developing a 25 nm nanoplatform composed of MnO_2, semiconducting $C_{43}H_{46}N_2S_3$ polymer and ORM (oxidase-responsive molecule) (PFODBT-MnOx-ORM) exhibited an oxidase-like activity dependent on the acidity of the environment that caused a 4-fold reduction in breast tumor volume without changing blood parameters (ALT, AST, ALP, BUN, and CREA) and a significant damage to major tissues. The highlights are improved FL intensity and PA signals in 4T1 xenograft tumor, which can be attributed to the oxidase-like activity of PFODBT-MnOx-ORM in the mildly acidic TME (pH 6 to 6.5). Therefore, the application of these nanozyme could result in achieving PA-FL dual-modal imaging in TME [101]. Recently, it was found that the mesoporous carbon-MnO_2 (MC-Mn) integrated with PDT/PTT through a dual-modal enzymatic reactions including oxidase-like activity by mesoporous carbon (MC-COOH) to generate H_2O_2 and a catalase-like activity to generate O_2 by MnO_2, in addition to reducing the 4T1 tumor volume by 9–11 times (71.5 % apoptosis rate) compared to monotherapy improves PA and MRI imaging intensity during treatment, especially 10 h following injection [102]. Despite the observed changes in the intensity of both T_1-weighted and T_2-weighted MRI signals 10 h after administration, the T_1-weighted MRI signal was significantly stronger than the T_2-weighted MRI signal. Regardless of dose- and time-dependent toxicity of the MC-Mn in 4T1

tumor cells and stability up to 10 h after injection in the blood and tumor tissue, no inflammation or toxicity was observed in the heart, kidney, lung, spleen and liver tissues. Concluded from and PA imaging, the rapid clearance rate of MC-Mn within 24 h is a major factor in reducing toxicity [102].

4. Coordinated structures of nanozymes in tumor imaging

While non-coordinated nanozymes have proven to yield satisfactory results in imaging, coordinated nanozymes attract tremendous attention in recent researches oriented to multimodal imaging-guided cancer therapy. Coordinated structures of nanozymes exhibit effectiveness in directly targeting tumors via metallic contrast agents or organic ligands, and indirectly through the delivery of contrast agents [103,104]. Utilizing the coordinated nanozymes with the synergistic ability of metal NPs and organic ligands in imaging and tuning their catalytic performance for controlled release of contrast agents should be further considered. However, despite the wide variety of coordinated structures, MOF groups, polymer-derived coordinated structures, and porous coordination cages are the most commonly used anticancer platforms with catalytic functionality, among which MOFs are known as the main target in imaging-guided cancer therapy.

4.1. MOF group

Easy production and long-term storage along with controllable degradability/toxicity and hepato-renal clearance have made the use of MOFs promising in therapeutic perspectives [105]. Among the MOFs, the MIL and ZIF groups are the most potential candidates in fulfilling imaging-guided cancer therapy.
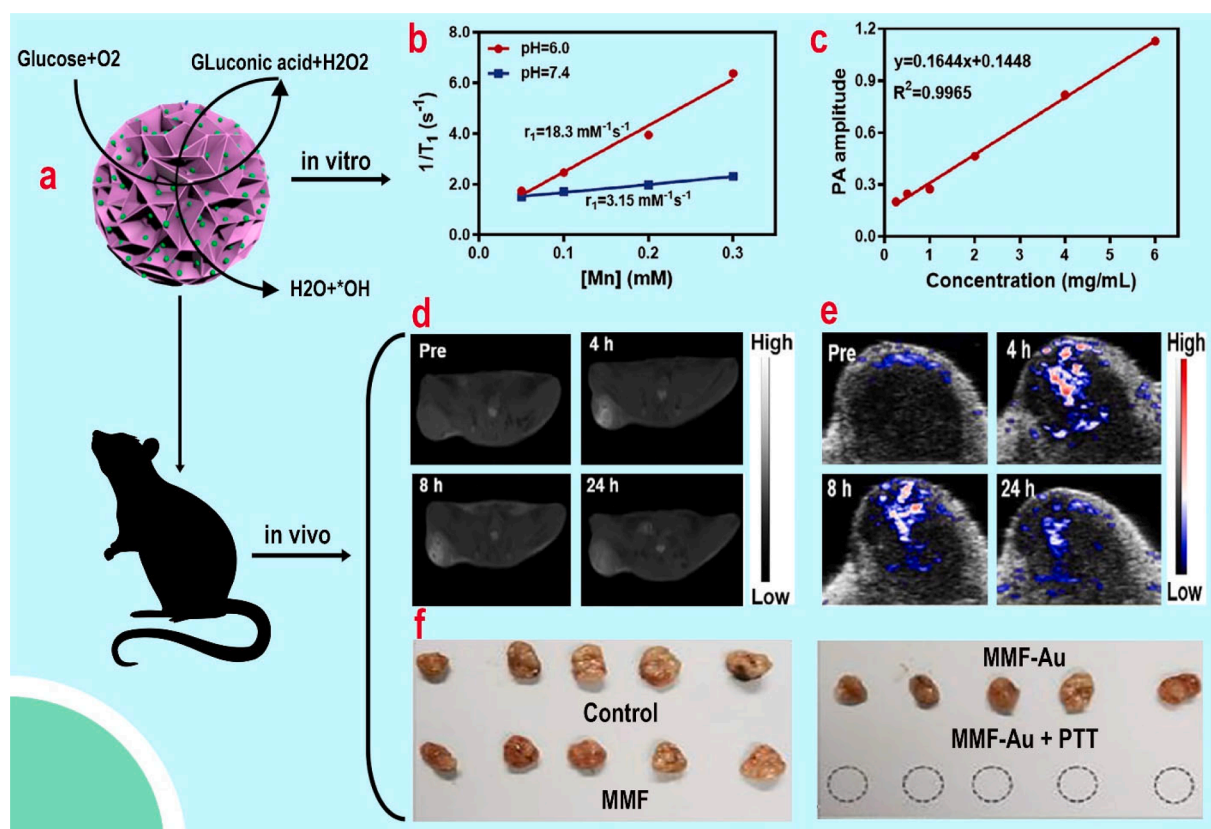

Fig. 4. Schematic representation of MMF-Au (Melanin-MnO_2-Au) function in OH production from low-H_2O_2 HeLa-tumors (a). Linear relationship of PA signal intensities with different concentrations of MMF-Au (b). The r_1 relaxivity of MMF-Au in pH 6.0 and 7.4 PBS buffer solution at 4 h incubation (c). MR images of HeLa-tumor-bearing mice pre- and post-intratumoral injection of MMF-Au (d). PA images of HeLa-tumor-bearing mice pre- and post-intratumoral injection of MMF-Au (e). Digital photos of excised tumors at day 20 (f). Reprinted with permission from Ref. [100], with permission from John Wiley. Copyright (2020) John Wiley.

4.1.1. MIL group

MIL structures are synthesized from inorganic elements with valence electrons and an organic compound with carboxyl functional groups. Excellent water stability, pore flexibility, and feasible synthesis via solvothermal, electrochemical, and ultrasonic methods, as well as the potential ability to combine with a wide range of nanozymes, have prompted researchers to expand the application of MLF-based structures in the development of anticancer and imaging platforms [106]. In this context, in order to deliver contrast agents and pharmaceutical compounds to Hela-tumor cells, Wang, Zhou, Chen, Shi, Wang, Lu, Zhao, Xia, Zhou and Liu [25] by developing a pH-responsive $Mn_3[Co(CN)_6]_2$@MIL-100(Fe) with a dimension of ~150 nm through the hydrothermal and layer-by-layer approaches could achieve targeted delivery. The MRI results from $Mn_3[Co(CN)_6]_2$@MIL-100(Fe) injection indicate enhanced T_1 and T_2 signal intensities and favorable changes in r_1 and r_2 compared to commercial contrast agents. It seems that the improvement in MRI signal strength is derived from two events: (1) increased contrast agent permeability due to increased O_2 by the catalase-like activity of manganese, and (2) formation of an outer magnetic layer affecting the longitudinal relaxation of water protons resulted from H_2O_2 decomposition. Furthermore, it was found that drug-containing MOF has superior positive T_1 compared to bare MOF due to the improvement of r_1 from 4.874 to 6.607 (mM/s). Meanwhile, the stability of MRI signal intensity in tumor tissue over 24 h indicates the enhanced EPR effect of $Mn_3[Co(CN)_6]_2$@MIL-100(Fe) in Hela-tumor. In addition to achieving improved imaging resolution, $Mn_3[Co(CN)_6]_2$@MIL-100(Fe) fulfilled the expectations of HeLa tumor therapy by reducing tumor weight by 5–7 fold mediated by ROS and targeted accumulation of artesunate derived from a tunable two-compartment drug release. Also, according to histopathological findings, no toxicity was observed in major tissues such as the liver, kidney, and spleen, despite dose-dependent toxicity in tumor cells. The pH-responsive drug release and promising degradation in physiological environment are most likely the primary reasons for the appreciated biocompatibility of $Mn_3[Co(CN)_6]_2$@MIL-100(Fe) [25]. Another study indicated that PEGylated Fe_3O_4@MIL-100(Fe)-UCNPs obtained by hydrothermal method and layer-by-layer approach were prominent for imaging-guided cancer therapy mediated by direct and indirect mechanisms [107]. A direct mechanism was suggested by catalytic release of metal ions to enhance Yb/Gd-CT contrast agent concentration with an increase in HU to 173.2 (slope 12.47 $\pm$ 0.35). While in the indirect mechanism, catalytic degradation of H_2O_2 to O_2 caused CT imaging clarity. Moreover, Fe_3O_4@MIL-100(Fe)-UCNPs-PEG integrated with PTT (980 nm, 0.9 W/cm^2 for 15 min) caused 5-fold and 7-fold reductions in U14-tumor volume compared to the non-irradiated and control groups, respectively, by amplifying the generation of $^{\cdot}O_2$ and $^{\cdot}OH$. On the other hand, the MTT and histopathology results demonstrated the high biocompatibility of Fe_3O_4@MIL-100(Fe)-UCNPs-PEG, explaining the non-toxicity of MOFs in L929 cells (over 90 % viability) and the absence of obvious signs of inflammation and necrosis in major tissues, respectively. Despite the significant toxicity of Fe_3O_4@MIL-100(Fe)-UCNPs-PEG in tumor tissue, the lack of toxicity in off-target tissues and normal cells is mediated by PEGylating and the high rate of Fe_3O_4@MIL-100(Fe)-UCNPs-PEG clearance from liver and kidney certified by CT imaging. In fact, reduction in the CT imaging signal intensity at 30–60 min indicates that the PEGylated MOFs were rapidly degraded and filtered [107]. Despite the low toxicity and relatively promising performance of nanocarriers in cancer therapy, the main challenge is their low stability in imaging-guided cancer therapy. For this purpose, through the development of PVP-coated MIL-100 containing ABTS, Liu and co-workers [10] improved the therapeutic performance and PA imaging by increasing the $^{\cdot}OH$ and O_2 levels mediated by peroxidase-like activity, in addition to extending the stabilization time of nanocarriers. They demonstrated that the peroxidase-like activity of ABTS@MIL-100/PVP amplified PA signals mediated by increased O_2 levels derived from H_2O_2 degradation in breast tumor cells. Furthermore, due to the H_2O_2-

reposnive behavior of ABTS@MIL-100/PVP, these nanozymes have been shown to detect small breast tumors (less than 20 mm3) through PA imaging. Removal of H_2O_2 from the medium by dimethylthiourea clearly confirmed the beneficial effects of ABTS@MIL-100/PVP on improving the PA signal intensity caused by the inhibition of peroxidase-like activity of developed platform. Furthermore, it was confirmed that the iron NPs in the organic framework generate oxidized ABTS in the vicinity of H_2O_2, which enhances the FL imaging of cancer cells. Along with imaging, the synergistic effect of MOF and PTT (10 min irradiation, 1.0 W/cm^2) improved the prospects for breast cancer treatment evidenced by reducing the breast tumor volume by 4–6 folds. Also, in contrast to the dose-dependent toxicity of ABTS@MIL-100/PVP in 4T1 cells, no clear signs of inflammation or necrosis were observed in the major tissues. The high clearance rate of ABTS@MIL-100/PVP as evidenced by the reduction in FL signal intensity and iron content in the kidney and liver within 24 h appears to be the main factor controlling toxicity, regardless of the surface modification of MOFs with polymers [10]. Recently, by loading PB on MIL-100, Chen, Li, Pan, Hu, Cheng and Zhang [26] were able to not only target 4T1 tumor but also detect lymph node metastases with high accuracy (Fig. 5A). In this study, the increased PA signal intensity at the wavelengths of 700–780 nm was expected due to the increased decomposition of H_2O_2 to $^{\cdot}OH$ and O_2 and its positive effect on increasing the release of Mn ion and other metal ions in the TME. Similarly, the release of Fe ion along with Mn ion shortened the relaxation time at pH 5–6 compared to pH 7.4 and improved T_1-weighted MRI performance. Assessment of PA signal differences and the changes in T_1-weighted MRI signal intensity in tumor tissues and lymph nodes compared to healthy tissues following 8 h of PB@MIL-100 injection, enabled the detection of cancer metastasis in lymph nodes (Fig. 5A). The release of Fe and Mn ions in the presence of H_2O_2 and mildly acidic TME may contribute to the improvement of catalytic cancer therapy mediated by ROS generation and enhanced light-to-heat conversion efficiency (from 35.5 °C to 51.2 °C in an acidic environment) in PTT (808 nm NIR laser: 1 W/cm^2, 6 min). Despite the effectiveness of MOF in reducing tumor weight by 5–7-fold combined with PTT or reducing tumor volume by 30 % combined with chemo-therapy, the outputs of histopathology and hematological parameters show that PB@MIL-100 does not cause any toxicity in the major tissues or changes in ALT, AST, BUN, and CREA despite its high accumulation in liver, spleen, kidney and lung tissue. Surface modification, degradation in the acidic TME, and the rapid clearance rate of PB@MIL-100 from the liver and kidney determined by low signal intensity of images within 24 h appear to be the main reason reflecting the reduced toxicity [26].

4.1.2. ZIF group

ZIFs are topologically similar to zeolites and are synthesized using metal ions with valence electrons and imidazole derivatives. Their use in biomedical fields is of particular interest due to their chemical and thermal stability, feasible fabrication, and affordable as well as simple synthesis routes achieved by hydrothermal and solvothermal approaches [108]. ZIFs are surprisingly effective in catalytic cancer therapy because of their independent enzyme-mimicking activity (e.g., oxidation and epoxidation), stability in biological and water environments, and degradability in TME [109]. For example, to achieve multimodal imaging, Pan and co-workers [27] designed a silicate-coated MOF (ZIF-8@mSiO$_2$) by growing Mn in situ to improve the performance of ULS and MRI imaging-guided breast cancer therapy mediated by dual-modal peroxidase/catalase-like activities (Fig. 5B). By increasing the O_2 content caused by the decomposition of H_2O_2, ZIF-8@mSiO$_2$ not only overcomes hypoxia and ensures higher permeability of the therapeutic compounds but also makes the generated O_2 available as a ULS imaging contrast agent during cancer therapy. This finding is supported by the fact that the presence of H_2O_2 increases the intensity of the ULS signal 30 min following injection by 9–10 folds, regardless of the acidity of the environment (Fig. 5B). Moreover, as expected, Mn ions that positively enhance T_1-weighted MRI signals caused visualization of tumors by
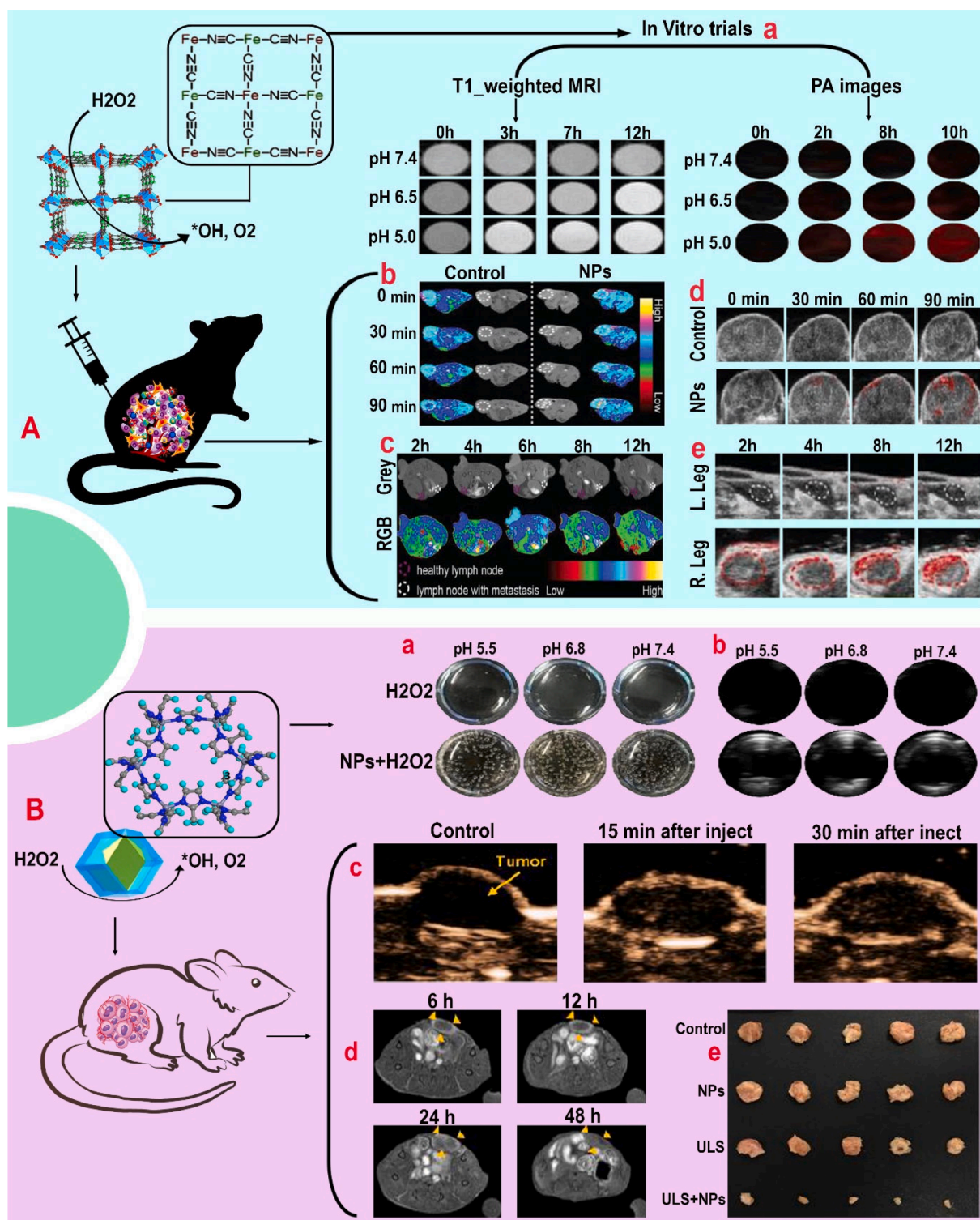
Fig. 5. A) Schematic view of the PB@MIL-100 nanozyme and assosiated effect on T_1-weighted MRI images and PA imaging *in vitro* at different times and various pH (7.4, 6.5, or 5.0) (a). T_1-weighted MRI images of 4T1-tumor bearing mice following injection with NPs (PB@MIL-100) (b). T_1-weighted MRI images of lymph nodes with and without metastasis at different times following injection of PB@MIL-100 (c). Corresponding PA images of 4T1-tumor bearing mice after injection of PB@MIL-100 (d). PA images of lymph nodes with and without metastasis at different times following injection of PB@MIL-100. White circle: the lymph nodes in the left leg. Red circle: the lymph nodes in the right leg (e). Reprinted with permission from Ref. [26], with permission from John Wiley. Copyright (2020) John Wiley. B) Schematic view of the ZIF-8@mSiO$_2$ and its effect on O$_2$ generation (a) and *in vitro* ULS imaging in the presence and absence of H$_2$O$_2$ at pH 5.5, 6.8 and 7.4 (b). *In vivo* ULS imaging before and following intratumoral injection of ZIF-8@mSiO$_2$ (1 mg/mL, 50 μL) (c). T_1-weighted MRI after intravenous injection of 20 mg/kg ZIF-8@mSiO$_2$. The circle in the bottom right corner is the control (d). Photographs of 4T1 tumor-bearing mice in different groups (Scale bar: 1 cm) (e). Reprinted with permission from Ref. [27], with permission from John Wiley. Copyright (2020) John Wiley. (For interpretation of the references to colour in this figure legend, the reader is referred to the web version of this article.)
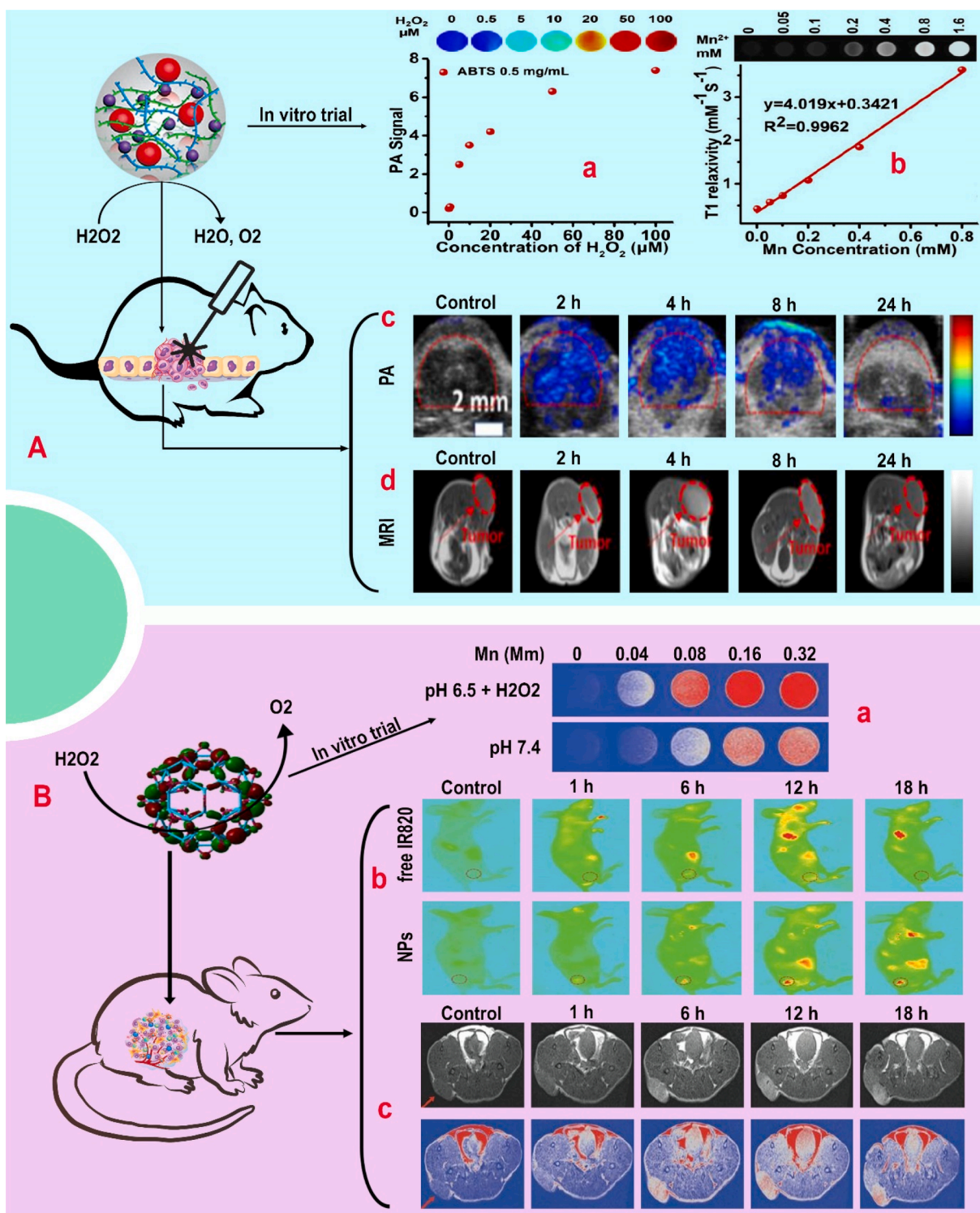
Fig. 6. A) PA images and PA signal intensities of Mn-ABTS-HRP-PEG dispersed in buffer with different H_2O_2 concentrations (a). MRI and T_1 relaxation rates of various concentrations of Mn-ABTS-HRP-PEG (b). *In vivo* PA imaging (c) and MRI (d) of CT26 tumor after intravenous injection of Mn-ABTS-HRP-PEG (200 μL). Reprinted with permission from Ref. [113], with permission from World Scientific. Copyright (2022) World Scientific. B) T_1-weighted MRI and longitudinal relaxation rate (r_1) of BSA-MnO$_2$/IR820@OCNCs (a). *In vivo* FL images of mice at indicated times after intravenous injection of free IR820 and BSA-MnO$_2$/IR820@OCNCs. Red circles indicate the region of the tumor (b). *In vivo* MR images of KYSE-30-tumor bearing mice at indicated time points following intravenous injection of BSA-MnO$_2$/IR820@OCNCs (c). Reprinted with permission from Ref. [116], with permission from Royal Society of Chemistry. Copyright (2022) Royal Society of Chemistry. (For interpretation of the references to colour in this figure legend, the reader is referred to the web version of this article.)

longitudinal relaxation of water protons generated from H_2O_2. The signals obtained at pH 5.5 and 6.8 are enhanced compared to pH 7.4 through the improvement of r_1 from 0.25 mM/s at pH 7.4 to 0.39 and 0.86 mM/s at pH 6.8 and 5.5, consistent with the enrichment of H_2O_2 in acidic environments. The 12 h' stability of MRI signal intensity in tumor tissue also showed a suitable EPR effect of ZIF-8@mSiO2, inhibiting tumor development by 92 %, especially in synergistic activity with SDT (1.0 MHz, 1 W/cm^2, 1 min, 50 % duty cycle), due to increased ROS generation stemmed from dual-modal peroxidase/catalase-like activities of these nanozymes. The main reason for the non-toxicity of ZIF-8@mSiO2, is the high clearance rate from liver and kidney tissues, as confirmed by a decrease in FL intensity in liver and kidney tissues at 12 h, which is consistent with MRI findings [27]. In another study, in order to enhance catalytic activities and imaging with minimal toxicity caused by surface modification, Ma et al. [110] developed a Zn-ZIF@PtAu-PEG nano-reactor with dimensions of 200–250 nm, which represented an important perspective in the treatment of breast cancer mediated by increasing ROS, overcoming hypoxia, converting light-to-heat with high efficiency, and PA-FL dual-modal imaging. Zn-ZIF@PtAu-PEG nano-structures enhance the PA signal intensity in two ways, including (1) indirectly via increasing the O_2 content generated by the decomposition of H_2O_2, and (2) directly by mediating the tumor accumulation of AuNPs and PtNPs. The PA signal intensity is gradually enhanced with increasing Zn-ZIF@PtAu-PEG concentration in a linear relationship (a slope of 1.6403) over 12 h, thus, by controlling the dose and circulation time of Zn-ZIF@PtAu-PEG, the PA signal can be tuned. On the other hand, the increase in PA signal intensity at pH 5–6 indicates the potential dual-modal peroxidase/catalase-like activities of Zn-ZIF@PtAu-PEG in the acidic TME, which can reflect the targeting and visualizing tumor tissues enabled by the fabricated nanozyme. Moreover, the presence of PA and FL signals up to 24 h shows that Zn-ZIF@PtAu-PEG has a significant EPR effect in tumor tissue. Additionally, MOF caused a 3- to 5-fold reduction in tumor weight, especially in combination with PTT. The decrease in the intensity of FL and PA signals at 12 h and their disappearance within 24 h confirms the Zn-ZIF@PtAu-PEG clearance. Furthermore, no significant changes in hematological parameters and morphological structure of tissues and normal COS7 cells indicated the high biocompatibility of Zn-ZIF@PtAu-PEG. Degradation of the MOF structure in an acidic microenvironment, PEGylation and release of NPs with a size of ~10 nm from the coordinated structure could effectively reduce the toxicity of the Zn-ZIF@PtAu-PEG [110]. Recently, Zheng et al. [28] were able to improve PA and FL imaging resolution up to 10-fold and 8.1-fold, respectively, with the application of zeolite-carbon-based NPs. They showed that zeolite-carbon NPs enhances the PA imaging resolution in the second radiation window, especially at a wavelength of 1064 nm, by (1) a 2-fold increase in O_2 levels mimicked by dual-modal peroxidase/catalase-like activities, and (2) accumulation in tumor tissue as a contrast agent. The rapid clearance rate of zeolite-carbon nanostructures from the hepatobiliary system and renal filtration is corroborated by the reduction of PA and FL signal intensity in the major tissues and the absence of cellular inflammation, necrosis and morphological changes within the tissue [28].

4.2. Coordination-derived polymers

These compounds are composed of natural/synthetic ligands such as nucleotides, proteins, polymers, polysaccharides, and various metals [111]. Depending on the properties of the components, they differ in mechanical strength, stability and processing [112]. These compounds have received promising attention due to their very low toxicity and controlled biodegradability despite the uncontrollable pore size. In this context, Zhao et al. [113] used a one-step self-assembly system to generate a 10–50 nm coordinated structure composed of ABTS, MnO_2, horseradish peroxidase (HRP), and PEG. Coordinated Mn-ABTS-HRP-PEG improves the PA and MRI imaging resolution through elevating O_2 levels mediated by catalase-like activity and Mn accumulation in

colon (CT26) and bladder (T24) cancer tissues (Fig. 6A). Based on the expected increase in PA signal intensity with increasing H_2O_2 concentration *in vitro*, 4 h after subcutaneous injection of Mn-ABTS-HRP-PEG, PA signal intensity reached a maximum in colon and bladder tumors derived from catalytic generation of O_2 (Fig. 6A). Similarly, Mn-ABTS-HRP-PEG injection and accumulation of Mn in the tumor tissue increased the MRI signal intensity and brightening contrast in tumor at 4 h. In spite of the accumulation of Mn-ABTS-HRP-PEG in the off-target tissues, the reduction and disappearance of PA and MRI signals intensity at 24 h (Fig. 6A) and the reduced Mn content in the major organs indicate a rapid clearance rate of Mn-ABTS-HRP-PEG. Also, the high levels of Mn in urine caused by Mn-ABTS-HRP-PEG degradation indicate the high biodegradability of these nanocarriers in major tissues [113]. Recently, another study developed a self-assembly strategy to promote O_2 within the tumor tissue depends on the coordination of L-cysteine and PVP-modified copper and molybdenum (MoO$_x$-Cu-Cys) with a dimension of ~95 nm [29]. The presence of Cu and Mo increased the affinity of nanozymes for catalytic degradation of H_2O_2 to O_2 in the acidic TME by 138-fold compared to Mo alone. The accumulation of Cu and Mo ions along with enhancement of O_2 and H_2O levels within the tumor improved the performance of T_1-weighted MRI by shortening the relaxation time of r_2 and improving r_1, in addition to 1.5–2.5-fold tumor reduction. However, due to the decreased Cu and Mo contents in major tissues and the reduced intensity of the MRI signal at 12 h, MoO$_x$-Cu-Cys was confirmed to have a high clearance rate from the liver and kidney. Faster degradation of cysteine network structure in biological environment and the use of PVP coatings and higher EPR effect of MoO$_x$-Cu-Cys nanostructures are believed to be the main factors controlling their toxicity. Meanwhile, the absence of inflammation, necrosis, or alterations in the morphological structure of cells in major tissues and the no differences in blood parameters (ALT, AST, ALP, BUN, and CREA) demonstrate the biocompatibility of MoO$_x$-Cu-Cys following application in 4T1-tumor catalytic therapy [29].

4.3. Porous organic cages

Recently, POC has attracted a great deal of attention in catalytic cancer therapy due to its regular porous structure, high surface area, and tunable physicochemical properties [114]. One of the most important materials in the synthesis of POC is carbon compounds. Despite the high toxicity of carbon, carbon-derived compounds have received a great deal of interest in the development of potential platforms for imaging-guided cancer therapy due to their high electrical conductivity, chemical stability, catalytic activity, and cost-effectiveness [115]. In this regard, Liu et al. [116] using hydrothermal and deposition methods, designed a BSA-MnO2/IR820@OCNCs with a dimension of ~114 nm in which MnO_2 enhances the resolution of MRI images through its catalytic activity in the TME (Fig. 6B). An enhanced MRI imaging resolution was observed due to T_1-weighted MRI signal enhancement derived from elevated Mn concentration and ion release from POC at pH 6.5 in the presence of H_2O_2. Interestingly, the increase in longitudinal relaxation r_1 from 1.83 (mM/s) at pH 7.4 to 9.28 (mM/s) at pH 6.5 in the presence of H_2O_2, as well as MnO_2's catalytic activity to generate H_2O and facilitate Mn ion access to water, are key parameters influencing the MRI imagining resolution. Moreover, increasing the O_2 content through MnO_2's catalase-like activity improves the permeability of IR820-containing POC and enhances imaging resolution, in addition to improving PTT/PDT. A 3-fold to 4-fold reduction in tumor weight, especially in synergy with PDT/PTT (0.8 W/cm^2 of 808-nm laser irradiation), along with high EPR effect ascertained by the presence of FL and MRI signals up to 18 h, confirming promising efficiency of BSA-MnO2/IR820@OCNCs in high IR820 permeability, POC retention and catalytic activity of MnO_2 in ROS generation. Despite the dose-dependent toxicity of POC in human esophageal carcinoma KYSE-30 cells, BSA-MnO2/IR820@OCNC caused no toxicity to normal cells and off-target tissues, and no changes in blood parameters. Potential

targeting ability of BSA-MnO$_2$/IR820@OCNC, high clearance rate from kidney and liver tissue, and finally feasible surface modification with BSA appear to be the main keys to controlling toxicity and improving biocompatibility [116]. Nevertheless, the lack of studies on the mechanism of carbon degradation in tissues and its clearance from the kidney and hepatobiliary system is a major challenge.

5. Which imaging agent: non-coordinated or coordinated nanozymes

Regardless of the more benefits of coordinated nanozymes compared to non-coordinated ones [117–120], which include (1) high capacity for simultaneous delivery of multiple therapeutic compounds and contrast agents; (2) controlled function by internal and external stimuli; (3) high diversity in composition and structure; (4) high biocompatibility; (5) conductivity and high targeting in cancer therapy and imaging; (6) long-term EPR effect in tumors; (7) high degradability, and (8) potential diversity, the use of coordinated nanozymes in imaging-guided catalytic cancer therapy is recommended. For instance, the toxicity levels in the main tissues were found to be significantly elevated with increasing time course of imaging when using nanozymes containing Fe such as Fe$_3$O$_4$@CS/CuS [80], FeWOX-PEG [83], SnFe$_2$O$_4$ [93], and Mn$_{0.95}$Fe$_{2.05}$O4 [96]. Despite using coatings like PEG, the non-coordinated nanozymes show higher toxicity compared to coordinated nanozymes such as Mn$_3$[Co(CN)$_6$]$_2$@MIL-100(Fe) [25] and Fe$_3$O$_4$@-MIL-100(Fe)-UCNPs-PEG [107] due to accumulation in off-target tissues (liver, lung, spleen, kidney), low filtration rate from kidney and liver stemmed from their large particle size as well as improper degradation. Furthermore, it was noted that non-coordinated nanozymes containing Au and Pt, such as PtSn@PEG [86], Au$_2$Pt-PEG-Ce6 [94], and Pd@Pt [95], effectively elevate the risk of toxicity by altering blood parameters, long-term accumulation in off-target tissues, and long-term filtration. Despite the reduction of toxicity through PEG coatings or the use of extrinsic stimulus such as sonodynamic for nanozyme activation in the target tissue, the non-coordinated nanozymes still show higher toxicity compared to Zn-ZIF@PtAu-PEG [110]. While Zn-ZIF@PtAu-PEG [110] provided a significant and stable signal to improve imaging. It was discovered that PB@MIL-100 [26] compared to AgPd PB [85], in addition to reduced toxicity, resulted in a stronger and more stable signal for imaging. The reduction of toxicity was assessed by the analysis of pathophysiological complications in main tissues and change in hematological indices. While liposomal and protein coatings can modulate the toxicity of non-coordinated nanozyme, their higher production cost and accumulation in main tissues making them less likely to consider their clinical use compared to coordinated nanozymes like ZIF-8@mSiO$_2$ [27] as shown in Ir@liposome [89] and BSA-IrO$_2$ [90]. In general, coordinated nanozymes exhibit greater potential in clinical applications in imaging than non-coordinated ones, according to published results.

6. Challenges and future perspectives

As discussed, nanoscale catalysts have attracted attention since 2002 as functional materials in biomedical implementations, mainly for diagnostic and therapeutic purposes. Although these compounds have been successful in the laboratory scale in diagnostic imaging and image-guided cancer therapy, their clinical use is still delayed due to the lack of comprehensive information on their physiological behavior. Although the catalytic activity of these compounds is controlled by external (light, sound, magnetic field,) and internal (H$_2$O$_2$, pH, substrate) stimuli, their unlimited activity in systems raises several challenges about their efficacy, kinetic parameters, stability, and degradation. It is clear that various modifiers, such as metal element ratios, stimuli, and coating can be used in modulation of the behavior of these platforms *in vivo*. However, whether these strategies can increase the potential biocompatibility and biodegradability of nanozymes with and without coordinated

structures is a major challenge that requires further investigations in future studies. Despite these drawbacks, the potential of nanozymes, with or without coordinated structure, in early cancer detection, drug delivery, and multimodal imaging-guided cancer therapy may result in the application of these compounds in the near future. Also, nanozymes can serve as smart nanostructures to target cancer with deep penetration depth for effective tumor treatment and imaging. In general, for the future application of nanozymes in therapeutic and imaging perspectives the following shortcomings should be taken into consideration (Fig. 7):

1- **Stimulated enzyme mimetic activity:** Despite the favorable selectivity of the substrate by nanozymes with and without coordinated structures and their catalytic performance *in vitro*, these compounds still could not mimic properly the native enzyme activity and efficiency *in vivo*. As a result, the challenges for incomplete degradation coupled with poor performance under a physiological environment make the use of these compounds complicated. Recently, the use of alloy-based nanozymes or the loading of different catalytic compounds into one platform, has been recommended to improve their sensitivity, selectivity, and performance.

2- **Manufacturing, characterization and scale-up production:** Although different strategies have been recommended for nanozyme preparation, the lack of a standard protocol for scale-up production remains a fundamental challenge in their commercialization and clinical application. Developing a database that optimizes synthesis techniques and taking into account aspects like surface modification, size control, and morphology to improve catalytic performance of nanozymes could help address these issues.

3- **Interfering reactions:** Some nanozymes have multiple enzymatic activities and tend to interact with different substrates, resulting in unlimited interfering reactions. In this regard, the use of external or internal activators/inhibitors as well as surface modification is expected to alleviate these challenges.

4- **The environmental impact:** The focus of the published papers in the field is on diagnosis, drug delivery and imaging of tumor cells. The environmental impact of nanozymes with and without coordinated structures is still unknown. In fact, nanozymes can interact unpredictably with other ambient materials, resulting in environmental safety issues. The use of highly controllable, degradable and smart compounds to enable us to guide and navigate nanozymes can effectively mitigate the aforementioned challenges.

5- *In vivo* **biodegradation and biocompatibility:** According to published papers, the biocompatibility of nanozymes with and without coordinated structure is directly related to their degradation rate over time. In long periods (30 days or more), we should pay further attention to the assessment of the aggregation and metabolization of nanozymes. Moreover, the majority of research publications have employed rodents *in vivo*, which is not an ideal model for physiological compatibility with human clinical applications. It seems that the use of three-dimensional bioprinted cancer models might provide important indicators of pharmacokinetics, absorption, distribution, toxicity, metabolism, duration of therapeutic effect, and clearance of nanozymes.

7. Conclusion

Over the last decade, the use of nanozymes, with or without coordinated structures, has proven to be highly effective in imaging-guided tumor therapy. Nanozymes have successfully improved imaging resolution by overcoming hypoxia levels and altering the chemical pattern of the TME through changes in O$_2$ or H$_2$O levels and the accumulation of metal ions. This has led to enhanced contrast agent penetration and signal-to-noise ratio. Additionally, nanozymes outperform contrast agents in addressing challenges such as accessing circulating cancer cells, detecting tumors smaller than 5 mm, imaging the edges of cancer
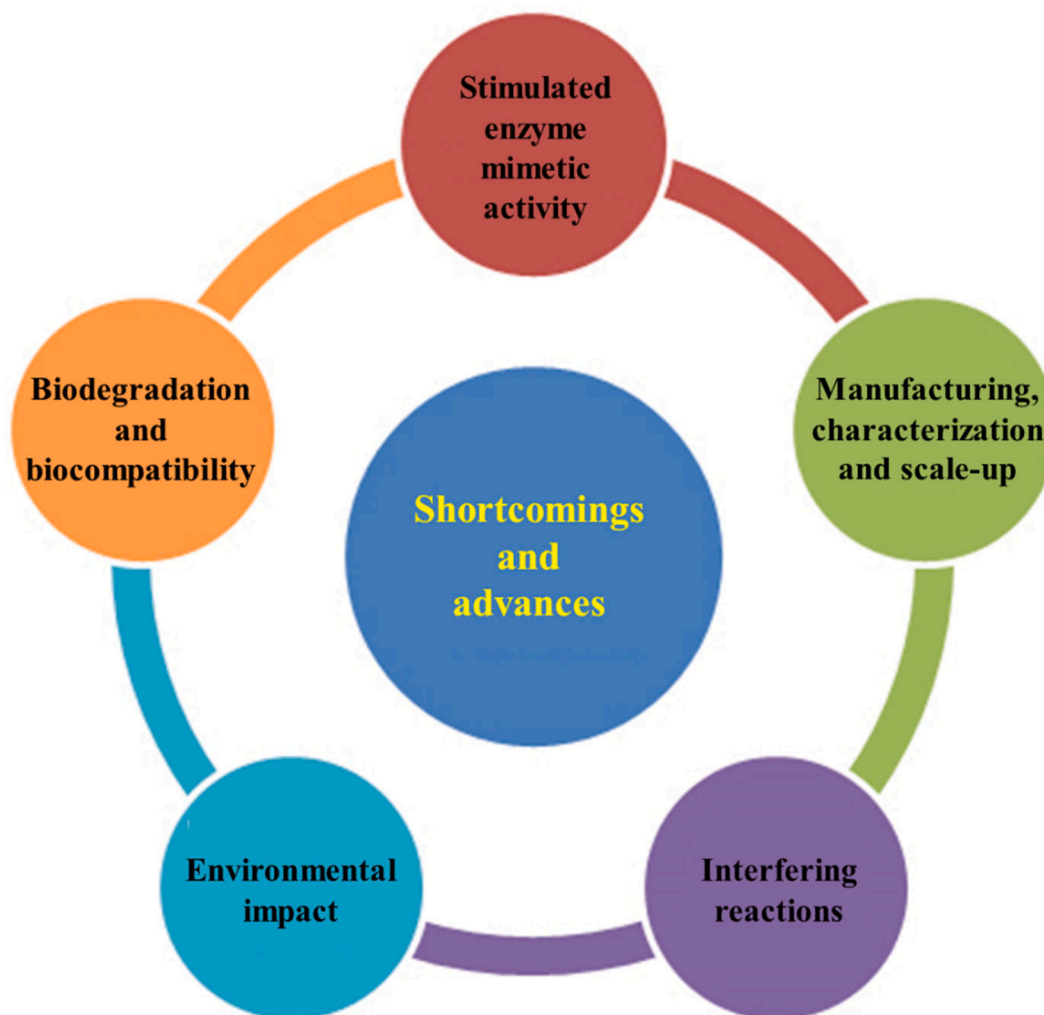
Fig. 7. The shortcoming and advances of using nanozymes with or without coordinated structures in catalytic imaging-guided cancer therapy.

tissue, and improving navigation in treatment and imaging. While it has been confirmed that nanozymes without coordinated structures potentially impact imaging resolution, they still face challenges such as non-targeted distribution, toxicity from continuous ion release, poor tunability, low drug and contrast agent loading, long-term retention in dimensions ≥20 nm, and unlimited catalytic activity. Coordinated structures not only address the above-mentioned concerns regarding non-coordinated structures but also have a greater impact on the imaging-guided tumor therapy process. This is achieved through increased porosity, high adaptability, extensive targeting capability with external and internal stimuli, multi-catalytic and multi-functional features, easy operation, and high biocompatibility. Nanozymes with a coordinated structure enables multimodal imaging-guided tumor therapy through the presence of various metal ions and fluorescent sensitive ligands (such as porphyrins), as well as carriers of various drugs and contrast agents. To support this claim, it was noted that using Mn^{2+} and Fe^{3+} ions to enhance T_1- and T_2-weighted MRI along with Zr as a CT contrast, can improve multimodal imaging enabled by coordinated nanozymes. However, there are significant challenges that limit the use of coordinated structure nanozymes, similar to non-coordinated structures, as imaging contrast agents. The main challenges include systemic toxicity derived from high accumulation and retention, low solubility in physiological fluids (zinc-carboxylate-derived coordinated structures), and affinity to biological ions (Zr affinity to phosphate). Moreover, the absence of a universal standard method for determining the optimal performance of nanozymes and the interfering reactions during

imaging-guided cancer therapy have restricted the use of nanozymes in clinical applications. The promising published results on the potential effects of nanozymes, particularly coordinated structures in multimodal imaging-guided cancer therapy, have raised the likelihood of their applications in clinical trials.

CRediT authorship contribution statement

Mojtaba Falahati: Conceptualization, Writing – original draft, Writing – review & editing, Visualization. **Majid Sharifi:** Conceptualization, Writing – original draft, Writing – review & editing, Visualization, Supervision. **Yasaman Vahdani:** Conceptualization, Writing – review & editing, Visualization. **Setareh Haghighat:** Conceptualization, Writing – review & editing, Visualization. **Timo L.M. ten Hagen:** Writing – original draft, Visualization, Supervision. **Yu Cai:** Conceptualization, Writing – review & editing, Visualization, Supervision.

Declaration of competing interest

The authors declare that they have no known competing financial interests or personal relationships that could have appeared to influence the work reported in this paper.

Data availability

No data was used for the research described in the article.

Acknowledgment

References

[1] L. Zhu, Y. Zhong, S. Wu, M. Yan, Y. Cao, N. Mou, G. Wang, D. Sun, W. Wu, Mater. Today Biol. 14 (2022) 100228.

[2] T. Zhang, S. Guo, F. Li, X. Lan, Y. Jia, J. Zhang, Y. Huang, X.-J. Liang, Adv. Drug Deliv. Rev. (2022) 114446.

[3] P. Li, D. Wang, J. Hu, X. Yang, Adv. Drug Deliv. Rev. 189 (2022) 114447.

[4] F. Wang, Y. Zhang, Z. Du, J. Ren, X. Qu, Nat. Commun. 9 (2018) 1209.

[5] M. Sharifi, W.C. Cho, A. Ansariesfahani, R. Tarharoudi, H. Malekisarvar, S. Sari, S.H. Bloukh, Z. Edis, M. Amin, J.P. Gleghorn, Cancers 14 (2022) 2868.

[6] Y. Shi, R. van der Meel, X. Chen, T. Lammers, Theranostics 10 (2020) 7921.

[7] E.D. Abdolahinia, M. Fathi, Z. Pirdel, S. Jafari, M. Samiei, K. Adibkia, F. Sefat, S. M. Dizaj, S. Sharifi, OpenNano (2022) 100100.

[8] Q. Luo, N. Shao, A.-C. Zhang, C.-F. Chen, D. Wang, L.-P. Luo, Z.-Y. Xiao, Pharmaceuticals 16 (2023) 249.

[9] Y. Huang, J. Ren, X. Qu, Chem. Rev. 119 (2019) 4357–4412.

[10] F. Liu, L. Lin, Y. Zhang, Y. Wang, S. Sheng, C. Xu, H. Tian, X. Chen, Adv. Mater. 31 (2019) 1902885.

[11] L. Teng, X. Han, Y. Liu, C. Lu, B. Yin, S. Huan, X. Yin, X.-B. Zhang, G. Song, Angew. Chem. Int. Ed. 60 (2021) 26142–26150.

[12] S. Liu, J. Xu, Y. Xing, T. Yan, S. Yu, H. Sun, J. Liu, View 3 (2022) 20200147.

[13] M. Chen, G. Deng, Y. He, X. Li, W. Liu, W. Wang, Z. Zhou, H. Yang, S. Yang, ACS Appl. Biol. Mater. 3 (2019) 639–647.

[14] D. Jana, D. Wang, A.K. Bindra, Y. Guo, J. Liu, Y. Zhao, ACS Nano 15 (2021) 7774–7782.

[15] S. Li, L. Shang, B. Xu, S. Wang, K. Gu, Q. Wu, Y. Sun, Q. Zhang, H. Yang, F. Zhang, Angew. Chem. 131 (2019) 12754–12761.

[16] Y. Xie, M. Wang, Q. Sun, D. Wang, S. Luo, C. Li, Inorg. Chem. 61 (2022) 6852–6860.

[17] Z. Nie, Y. Vahdani, W.C. Cho, S.H. Bloukh, Z. Edis, S. Haghighat, M. Falahati, R. Kheradmandi, L.A. Jaragh-Alhadad, M. Sharifi, Arab. J. Chem. 15 (2022) 103966.

[18] M. Sharifi, R. Kheradmandi, M. Alizadeh, Cancer Nanotechnol. 14 (2023) 1–20.

[19] W. Wu, L. Huang, E. Wang, S. Dong, Chem. Sci. 11 (2020) 9741–9756.

[20] C. Wang, H. Wang, B. Xu, H. Liu, View 2 (2021) 20200045.

[21] G. Tang, J. He, J. Liu, X. Yan, K. Fan, in: Exploration, Wiley Online Library, 2021, pp. 75-89.

[22] A. Bieniek, A.P. Terzyk, M. Wiśniewski, K. Roszek, P. Kowalczyk, L. Sarkisov, S. Keskin, K. Kaneko, Prog. Mater. Sci. 117 (2021) 100743.

[23] X. Niu, X. Li, Z. Lyu, J. Pan, S. Ding, X. Ruan, W. Zhu, D. Du, Y. Lin, Chem. Commun. 56 (2020) 11338–11353.

[24] W. Yang, X. Yang, L. Zhu, H. Chu, X. Li, W. Xu, Coord. Chem. Rev. 448 (2021) 214170.

[25] D. Wang, J. Zhou, R. Chen, R. Shi, C. Wang, J. Lu, G. Zhao, G. Xia, S. Zhou, Z. Liu, Chem. Mater. 29 (2017) 3477–3489.

[26] Y. Chen, Z.H. Li, P. Pan, J.J. Hu, S.X. Cheng, X.Z. Zhang, Adv. Mater. 32 (2020) 2001452.

[27] X. Pan, W. Wang, Z. Huang, S. Liu, J. Guo, F. Zhang, H. Yuan, X. Li, F. Liu, H. Liu, Angew. Chem. 132 (2020) 13659–13663.

[28] Z. Zheng, Z. Jia, Y. Qin, R. Dai, X. Chen, Y. Ma, X. Xie, R. Zhang, Small 17 (2021) 2103252.

[29] J. Zhou, D. Xu, G. Tian, Q. He, X. Zhang, J. Liao, L. Mei, L. Chen, L. Gao, L. Zhao, J. Am. Chem. Soc. 145 (2023) 4279–4293.

[30] W. Cai, H. Gao, C. Chu, X. Wang, J. Wang, P. Zhang, G. Lin, W. Li, G. Liu, X. Chen, ACS Appl. Mater. Interfaces 9 (2017) 2040–2051.

[31] H. Yang, Y. Xie, X. Zhong, L. Li, Inorg. Chem. Commun. 150 (2023) 110522.

[32] X. Gao, Y. Wang, G. Ji, R. Cui, Z. Liu, CrstEngComm 20 (2018) 1087–1093.

[33] S. Haddad, I. Abánades Lázaro, M. Fantham, A. Mishra, J. Silvestre-Albero, J. W. Osterrieth, G.S. Kaminski Schierle, C.F. Kaminski, R.S. Forgan, D. Fairen-Jimenez, J. Am. Chem. Soc. 142 (2020) 6661–6674.

[34] Y. Meng, D. Zhang, X. Chen, Z. Dai, X. Yao, P. Cui, D. Yu, G. Zhang, X. Zheng, ACS Appl. Nano Mater. 3 (2020) 4494–4503.

[35] S.-S. Wan, Q. Cheng, X. Zeng, X.-Z. Zhang, ACS Nano 13 (2019) 6561–6571.

[36] Y.M. Wang, W. Liu, X.B. Yin, Adv. Funct. Mater. 26 (2016) 8463–8470.

[37] D.K. Patel, R. Kesharwani, V. Kumar, 7 - Nanoparticles: an emerging platform for medical imaging, in: S.C.B. Gopinath, F. Gang (Eds.), Nanoparticles in Analytical and Medical Devices, Elsevier, 2021, pp. 113–126.

[38] D. Jiang, D. Ni, Z.T. Rosenkrans, P. Huang, X. Yan, W. Cai, Chem. Soc. Rev. 48 (2019) 3683–3704.

[39] C. Cao, N. Yang, X. Wang, J. Shao, X. Song, C. Liang, W. Wang, X. Dong, Coord. Chem. Rev. 491 (2023) 215245.

[40] J. Tang, C. Huang, Y. Liu, T. Wang, M. Yu, H. Hao, W. Zeng, W. Huang, J. Wang, M. Wu, Coord. Chem. Rev. 490 (2023) 215211.

[41] X. Li, R. Yue, G. Guan, C. Zhang, Y. Zhou, G. Song, in: Exploration, Wiley Online Library, 2023, pp. 20220002.

[42] H. Wu, F. Xia, L. Zhang, C. Fang, J. Lee, L. Gong, J. Gao, D. Ling, F. Li, Adv. Mater. 34 (2022) 2108348.

[43] S. Wang, Y. Zhao, Y. Xu, Visual Computing for Industry, Biomedicine, and Art, 3 (2020) 1-12.

[44] F. Liu, H. Jang, R. Kijowski, T. Bradshaw, A.B. McMillan, Radiology 286 (2018) 676–684.

[45] J.J. Vaquero, P. Kinahan, Annu. Rev. Biomed. Eng. 17 (2015) 385–414.

[46] J. Li, K. Pu, Chem. Soc. Rev. 48 (2019) 38–71.

[47] Y. Kenry, B.L. Duan, Adv. Mater. 30 (2018) 1802394.

[48] N.L.S.T.R. Team, N. Engl. J. Med. 368 (2013) 1980–1991.

[49] J. Cao, B. Qiao, Y. Luo, C. Cheng, A. Yang, M. Wang, X. Yuan, K. Fan, M. Li, Z. Wang, Biomater. Sci. 8 (2020) 6561–6578.

[50] Y. Liu, X. Yang, Z. Huang, P. Huang, Y. Zhang, L. Deng, Z. Wang, Z. Zhou, Y. Liu, H. Kalish, Angew. Chem. Int. Ed. 55 (2016) 15297–15300.

[51] Y. Mantri, J.V. Jokerst, ACS Nano 14 (2020) 9408–9422.

[52] S. Zhu, R. Tian, A.L. Antaris, X. Chen, H. Dai, Adv. Mater. 31 (2019) 1900321.

[53] K.V. Keu, T.H. Witney, S. Yaghoubi, J. Rosenberg, A. Kurien, R. Magnusson, J. Williams, F. Habte, J.R. Wagner, S. Forman, Sci. Transl. Med. 9 (2017) eaag2196.

[54] R. García-Figueiras, S. Baleato-González, A.R. Padhani, A. Marhuenda, A. Luna, L. Alcalá, A. Carballo-Castro, A. Álvarez-Castro, Insights Imaging 7 (2016) 285–309.

[55] C. Li, G. Chen, Y. Zhang, F. Wu, Q. Wang, J. Am. Chem. Soc. 142 (2020) 14789–14804.

[56] B.A. Kairdolf, X. Qian, S. Nie, Anal. Chem. 89 (2017) 1015–1031.

[57] B.R. Smith, S.S. Gambhir, Chem. Rev. 117 (2017) 901–986.

[58] S. Khan, M. Sharifi, S.H. Bloukh, Z. Edis, R. Siddique, M. Falahati, Talanta 224 (2021) 121805.

[59] X. Zhang, Y. Liu, J. Doungchawee, L.J. Castellanos-García, K.N. Sikora, T. Jeon, R. Goswami, S. Fedeli, A. Gupta, R. Huang, J. Control. Release 357 (2023) 31–39.

[60] M. Sharifi, S.H. Hosseinali, P. Yousefvand, A. Salihi, M.S. Shekha, F.M. Aziz, A. JouyaTalaei, A. Hasan, M. Falahati, Mater. Sci. Eng. C 108 (2020) 110422.

[61] J. Li, Y. Zhou, S. Yan, W. Wu, M. Sharifi, Arab. J. Chem. 16 (2023) 105229.

[62] Q. Li, T. Wu, X. Fan, X. Guo, W. Jiang, K. Fan, Mater. Des. 224 (2022) 111430.

[63] L. Su, S. Qin, Z. Xie, L. Wang, K. Khan, A.K. Tareen, D. Li, H. Zhang, Coord. Chem. Rev. 473 (2022) 214784.

[64] S. Khan, M.M.N. Babadaei, A. Hasan, Z. Edis, F. Attar, R. Siddique, Q. Bai, M. Sharifi, M. Falahati, J. Adv. Res. 33 (2021) 227–239.

[65] M. Liang, X. Yan, Acc. Chem. Res. 52 (2019) 2190–2200.

[66] W. Zeng, M. Yu, T. Chen, Y. Liu, Y. Yi, C. Huang, J. Tang, H. Li, M. Ou, T. Wang, Adv. Sci. 9 (2022) 2201703.

[67] T. Chen, W. Zeng, Y. Liu, M. Yu, C. Huang, Z. Shi, C. Lin, J. Tang, L. Mei, M. Wu, Small 18 (2022) 2202964.

[68] R. Yang, S. Fu, R. Li, L. Zhang, Z. Xu, Y. Cao, H. Cui, Y. Kang, P. Xue, Theranostics 11 (2021) 107.

[69] Z. Wang, Z. Li, Z. Sun, S. Wang, Z. Ali, S. Zhu, S. Liu, Q. Ren, F. Sheng, B. Wang, Sci. Adv. 6 (2020) eabc8733.

[70] S. Dong, Y. Dong, T. Jia, S. Liu, J. Liu, D. Yang, F. He, S. Gai, P. Yang, J. Lin, Adv. Mater. 32 (2020) 2002439.

[71] J. Yu, F. Zhao, W. Gao, X. Yang, Y. Ju, L. Zhao, W. Guo, J. Xie, X.-J. Liang, X. Tao, ACS Nano 13 (2019) 10002–10014.

[72] P. Xu, X. Wang, T. Li, H. Wu, L. Li, Z. Chen, L. Zhang, Z. Guo, Q. Chen, Nanoscale 12 (2020) 4051–4060.

[73] Z.-H. Li, Y. Chen, Y. Sun, X.-Z. Zhang, ACS Nano 15 (2021) 5189–5200.

[74] M. Zhang, B. Li, Y. Du, G. Zhou, Y. Tang, Y. Shi, B. Zhang, Z. Xu, Q. Huang, Chem. Eng. J. 424 (2021) 130356.

[75] Z. Yin, Q. Ji, D. Wu, Z. Li, M. Fan, H. Zhang, X. Zhao, A. Wu, L. Cheng, L. Zeng, ACS Appl. Mater. Interfaces 13 (2021) 14928–14937.

[76] S. Fu, R. Yang, L. Zhang, W. Liu, G. Du, Y. Cao, Z. Xu, H. Cui, Y. Kang, P. Xue, Biomaterials 257 (2020) 120279.

[77] D. Wang, W. Fang, C. Huang, Z. Chen, T. Nie, J. Wang, L. Luo, Z. Xiao, Smart Mater. Med. 3 (2022) 159–167.

[78] S. Thangudu, C.-H. Su, Biomolecules 11 (2021) 1015.

[79] M. Li, H. Zhang, Y. Hou, X. Wang, C. Xue, W. Li, K. Cai, Y. Zhao, Z. Luo, Nanoscale Horiz. 5 (2020) 202–217.

[80] K. Zhang, Z. Yang, X. Meng, Y. Cao, Y. Zhang, W. Dai, H. Lu, Z. Yu, H. Dong, X. Zhang, Mater. Chem. Front. 2 (2018) 1184–1194.

[81] H. Ding, Y. Cai, L. Gao, M. Liang, B. Miao, H. Wu, Y. Liu, N. Xie, A. Tang, K. Fan, X. Yan, G. Nie, Nano Lett. 19 (2019) 203–209.

[82] Y. Han, J. Ouyang, Y. Li, F. Wang, J.-H. Jiang, ACS Appl. Mater. Interfaces 12 (2020) 288–297.

[83] F. Gong, N. Yang, Y. Wang, M. Zhuo, Q. Zhao, S. Wang, Y. Li, Z. Liu, Q. Chen, L. Cheng, Small 16 (2020) 2003496.

[84] H. Veroniaina, Z. Wu, X. Qi, J. Adv. Res. 33 (2021) 201–213.

[85] T. Jia, D. Li, J. Du, X. Fang, V. Gerasimov, H. Ågren, G. Chen, J. Nanobiotechnol. 20 (2022) 1–19.

[86] Y. Zhu, R. Zhao, L. Feng, C. Wang, S. Dong, M.V. Zyuzin, A. Timin, N. Hu, B. Liu, P. Yang, ACS Nano 17 (2023) 6833–6848.

[87] Q. Liu, X. Zhu, L. Zhong, S. Zhang, X. Luo, Q. Liu, L. Tang, Y. Lu, Environ. Sci. Nano 9 (2022) 1212–1235.

[88] D. Xu, L. Wu, H. Yao, L. Zhao, Small 18 (2022) 2203400.

[89] L. Feng, Z. Dong, C. Liang, M. Chen, D. Tao, L. Cheng, K. Yang, Z. Liu, Biomaterials 181 (2018) 81–91.

[90] W. Zhen, Y. Liu, L. Lin, J. Bai, X. Jia, H. Tian, X. Jiang, Angew. Chem. 130 (2018) 10466–10470.

[91] Q. Dan, D. Hu, Y. Ge, S. Zhang, S. Li, D. Gao, W. Luo, T. Ma, X. Liu, H. Zheng, Biomater. Sci. 8 (2020) 973–987.

[92] L. Zeng, H. Cheng, Y. Dai, Z. Su, C. Wang, L. Lei, D. Lin, X. Li, H. Chen, K. Fan, ACS Appl. Mater. Interfaces 13 (2020) 233–244.

[93] L. Feng, B. Liu, R. Xie, D. Wang, C. Qian, W. Zhou, J. Liu, D. Jana, P. Yang, Y. Zhao, Adv. Funct. Mater. 31 (2021) 2006216.

[94] M. Wang, M. Chang, Q. Chen, D. Wang, C. Li, Z. Hou, J. Lin, D. Jin, B. Xing, Biomaterials 252 (2020) 120093.

[95] D. Sun, X. Pang, Y. Cheng, J. Ming, S. Xiang, C. Zhang, P. Lv, C. Chu, X. Chen, G. Liu, ACS Nano 14 (2020) 2063–2076.

[96] S. Carregal-Romero, A.B. Miguel-Coello, L. Martínez-Parra, Y. Martí-Mateo, P. Hernansanz-Agustín, Y. Fernández-Afonso, S. Plaza-García, L. Gutiérrez, M.d. M. Muñoz-Hernández, J. Carrillo-Romero, Small 18 (2022) 2106570.

[97] H. Wang, Y. Shen, L. Chen, K. Li, Y. Shi, Z. Xu, D. Li, H. Chen, W. Wang, L. Gao, Mater. Today Nano 22 (2023) 100326.

[98] Y. Yao, Z. Wang, Q. Cao, H. Li, S. Ge, J. Liu, P. Sun, Z. Liu, Y. Wu, W. Wang, ACS Appl. Mater. Interfaces 14 (2022) 17153–17163.

[99] Y. Zu, H. Yao, Y. Wang, L. Yan, Z. Gu, C. Chen, L. Gao, W. Yin, View 2 (2021) 20200188.

[100] C. Jiang, T. He, Q. Tang, J. He, Q. Ren, D.-Y. Zhang, B. Gurram, N.T. Blum, Y. Chen, P. Huang, Appl. Mater. Today 26 (2022) 101357.

[101] L. Teng, X. Han, Y. Liu, C. Lu, B. Yin, S. Huan, X. Yin, X.B. Zhang, G. Song, Angew. Chem. 133 (2021) 26346–26354.

[102] J. Lu, Y. Mao, S. Feng, X. Li, Y. Gao, Q. Zhao, S. Wang, Acta Biomater. 148 (2022) 310–322.

[103] Z. Zhang, W. Sang, L. Xie, Y. Dai, Coord. Chem. Rev. 399 (2019) 213022.

[104] S. Khan, M. Falahati, W.C. Cho, Y. Vahdani, R. Siddique, M. Sharifi, L.A. Jaragh-Alhadad, S. Haghighat, X. Zhang, T.L. Ten Hagen, Adv. Colloid Interface Sci. (2023) 103007.

[105] S. Mallakpour, E. Nikkhoo, C.M. Hussain, Coord. Chem. Rev. 451 (2022) 214262.

[106] S. Yang, X. Li, G. Zeng, M. Cheng, D. Huang, Y. Liu, C. Zhou, W. Xiong, Y. Yang, W. Wang, Coord. Chem. Rev. 438 (2021) 213874.

[107] X. Wang, J. Xu, D. Yang, C. Sun, Q. Sun, F. He, S. Gai, C. Zhong, C. Li, P. Yang, Chem. Eng. J. 354 (2018) 1141–1152.

[108] Q. Wang, Y. Sun, S. Li, P. Zhang, Q. Yao, RSC Adv. 10 (2020) 37600–37620.

[109] S. Kouser, A. Hezam, M.N. Khadri, S.A. Khanum, J. Porous Mater. 29 (2022) 663–681.

[110] Z. Ma, M.F. Foda, H. Liang, Y. Zhao, H. Han, Adv. Funct. Mater. 31 (2021) 2103765.

[111] S. Suárez-García, R. Solórzano, F. Novio, R. Alibés, F. Busqué, D. Ruiz-Molina, Coord. Chem. Rev. 432 (2021) 213716.

[112] Z. Lin, J.J. Richardson, J. Zhou, F. Caruso, Nat. Rev. Chem. 7 (2023) 273–286.

[113] J. Zhao, F. Gong, N. Yang, H. Lei, Z. Han, Y. Yang, L. Cheng, J. Innov. Opt. Health Sci. 15 (2022) 2250026.

[114] D. Hu, J. Zhang, M. Liu, Chem. Commun. 58 (2022) 11333–11346.

[115] X. Yang, Z. Ullah, J.F. Stoddart, C.T. Yavuz, Chem. Rev. 123 (2023) 4602–4634.

[116] J. Liu, J. Gao, A. Zhang, Y. Guo, S. Fan, Y. He, K. Yang, J. Wang, D. Cui, Y. Cheng, Nanoscale 12 (2020) 21674–21686.

[117] B. Xu, S. Li, L. Zheng, Y. Liu, A. Han, J. Zhang, Z. Huang, H. Xie, K. Fan, L. Gao, Adv. Mater. 34 (2022) 2107088.

[118] M. Falahati, M. Sharifi, T.L. Ten Hagen, J. Nanobiotechnol. 20 (2022) 1–26.

[119] D. Wang, D. Jana, Y. Zhao, Acc. Chem. Res. 53 (2020) 1389–1400.

[120] L. Zheng, F. Wang, C. Jiang, S. Ye, J. Tong, P. Dramou, H. He, Coord. Chem. Rev. 471 (2022) 214760.